Subdiffractional tracking of internalized molecules reveals heterogeneous motion states of synaptic vesicles

Merja Joensuu,[1,2] Pranesh Padmanabhan,[2] Nela Durisic,[2] Adekunle T.D. Bademosi,[1,2] Elizabeth Cooper-Williams,[2] Isabel C. Morrow,[1,2] Callista B. Harper,[1,2] WooRam Jung,[3,4] Robert G. Parton,[3,4] Geoffrey J. Goodhill,[2,5] Andreas Papadopulos,[1,2] and Frédéric A. Meunier[1,2]

[1]Clem Jones Centre for Ageing Dementia Research, [2]Queensland Brain Institute, [3]Institute for Molecular Bioscience, [4]Centre for Microscopy and Microanalysis, and [5]School of Mathematics and Physics, The University of Queensland, Brisbane, Queensland 4072, Australia

Our understanding of endocytic pathway dynamics is severely restricted by the diffraction limit of light microscopy. To address this, we implemented a novel technique based on the subdiffractional tracking of internalized molecules (sdTIM). This allowed us to image anti–green fluorescent protein Atto647N-tagged nanobodies trapped in synaptic vesicles (SVs) from live hippocampal nerve terminals expressing vesicle-associated membrane protein 2 (VAMP2)–pHluorin with 36-nm localization precision. Our results showed that, once internalized, VAMP2–pHluorin/Atto647N–tagged nanobodies exhibited a markedly lower mobility than on the plasma membrane, an effect that was reversed upon restimulation in presynapses but not in neighboring axons. Using Bayesian model selection applied to hidden Markov modeling, we found that SVs oscillated between diffusive states or a combination of diffusive and transport states with opposite directionality. Importantly, SVs exhibiting diffusive motion were relatively less likely to switch to the transport motion. These results highlight the potential of the sdTIM technique to provide new insights into the dynamics of endocytic pathways in a wide variety of cellular settings.

Introduction

Although live fluorescence microscopy has played a key part in deciphering the different mechanisms underpinning the endocytic pathway, one of its limitations is the diffraction of light, which restricts imaging to cellular structures >200 nm in diameter (Li et al., 2015). A large fraction of endocytic structures are subdiffractional and, in some specialized cells such as neurons, these can constitute a considerable proportion of the cell volume. Developing adequate superresolution techniques to unravel the dynamic nature of subdiffractional endocytic structures is therefore warranted.

Synaptic vesicles (SVs) are 45-nm endocytic structures that are typically located in nerve terminals. They contain, and are able to release, neurotransmitters upon exocytic fusion with the plasma membrane at specific sites called active zones, thereby mediating fast neuronal communication (Couteaux and Pécot-Dechavassine, 1974; Südhof, 2012). Several SVs undergo fast recycling (Ryan et al., 1993; Pyle et al., 2000; Sankaranarayanan and Ryan, 2000; Gandhi and Stevens, 2003) and are capable of undergoing endocytosis, docking, and priming, thereby regaining fusion competence in a short period of time. Although the development of pH-sensitive markers has provided a wealth of information on SV recycling (Kavalali and Jorgensen, 2014), the sequence of the molecular interactions that control the recycling process has remained unclear because of the scarcity of methods that allow direct visualization of SVs in the crowded environment of the presynapse. Advances in superresolution methods have allowed the visualization and tracking of individual recycling SVs (Lemke and Klingauf, 2005; Shtrahman et al., 2005; Yeung et al., 2007; Westphal et al., 2008); however, the results obtained in these studies have relied on a limited number of trajectories from spatially isolated SVs, excluding discrete diffusional and transport states. Defining these mobility states is critical to our understanding of the intra- and intermolecular interactions that control both docking and priming, as changes in their dynamics underpin these essential processes.

Correspondence to Frederic A. Meunier: f.meunier@uq.edu.au; or Andreas Papadopulos: a.papadopulos@outlook.com

C.B. Harper's present address is Centre for Integrative Physiology, University of Edinburgh, Edinburgh EH8 9XD, Scotland, UK.

Abbreviations used: AUC, area under the mean square displacement curve; DIV, days in vitro; GNT, GFP nanotrap; HMM, hidden Markov model; MSD, mean square displacement; MSS, moment scaling spectrum; sdTIM, subdiffractional tracking of internalized molecules; SV, synaptic vesicle; uPAINT, Universal Point Accumulation Imaging in Nanoscale Topography; VAMP2, vesicle-associated membrane protein 2.

The Rockefeller University Press $30.00
J. Cell Biol. Vol. 215 No. 2 277–292
https://doi.org/10.1083/jcb.201604001

In this study, we describe a method based on a pulse-chase of fluorescently tagged ligands destined to undergo endocytic transport, which we have termed subdiffractional tracking of internalized molecules (sdTIM). Using this technique, we were able to image a large number of SVs simultaneously in active zones of live hippocampal neurons with unprecedented 36-nm precision. This in turn allowed us to image the activity-dependent internalization of anti-GFP Atto647N-tagged nanobodies bound to pHluorin-tagged vesicle-associated membrane protein 2 (VAMP2) to study the mobility of recycling SVs in live hippocampal nerve endings. As a proof of concept, we demonstrated that the mobility of internalized VAMP2–pHluorin–bound anti-GFP Atto647N-tagged nanobodies was significantly lower than that of those transiting the plasma membrane (Giannone et al., 2010). We also investigated the changes in SV mobility elicited upon restimulation and showed that the mobility of SVs in presynapses, but not in the adjacent axons, increased significantly. In addition to classical mean square displacement (MSD) and diffusion coefficient characterization of SV mobility, we also accounted for nonlinear diffusion by using a combination of single-particle tracking, the moment scaling spectrum (MSS), and Bayesian model selection applied to hidden Markov modeling (HMM). By investigating these anomalous and subdiffusive events, we were able to annotate heterogeneous mobility along a single SV trajectory and discovered that, in most nerve terminals, SVs stochastically switch between either purely diffusive and/or transport mobility states. We detected similar mobility patterns upon restimulation of internalized VAMP2–pHluorin–bound anti-GFP Atto647N-tagged nanobodies. Our results highlight the power of sdTIM in studying the entire SV recycling process and the potential of the technique to be applied to investigate other subdiffractional endocytic events.

Results

Subdiffractional imaging of internalized single molecules in live hippocampal neurons

The sdTIM technique uses fluorescently labeled single molecules to track the internalization of extracellular ligands, allowing high-density single-particle tracking of relatively long trajectories. Implementation of this technique requires the use of an adjusted oblique illumination laser angle, just slightly smaller than the critical angle required for total internal reflection fluorescence microscopy to optimize synaptic access (Fig. 1 A). We first applied sdTIM to live hippocampal neurons from rats to assess the mobility of internalized vesicular proteins after their activity-dependent translocation to the plasma membrane and subsequent endocytic internalization. Like many other vesicular proteins, VAMP2 is rapidly internalized in recycling SVs (Harper et al., 2016) and has been shown to exhibit similar mobility to that of other major SV proteins, such as synaptophysin and synaptotagmin 1 (Gimber et al., 2015). Importantly, the kinetics of SV recycling are not affected by VAMP2–pHluorin overexpression in neurons, as demonstrated by comparing the kinetics of antibody-labeled endogenous SV proteins and pH-sensitive SV markers (Hua et al., 2011). To image single SVs using sdTIM (Fig. 1 B), hippocampal neurons growing on glass-bottom dishes were transfected at 14–17 d in vitro (DIV) with VAMP2–pHluorin for 24 h (Fig. 1 C) and then simulated with high K^+ buffer in the presence of anti-GFP Atto-647N–tagged nanobodies (Atto647N nanobodies) for 5 min. pHluorin is a variant of GFP, the fluorescence of which is quenched in the acidic environment of the SV and becomes unquenched upon fusion with the plasma membrane (Miesenböck et al., 1998). The 5-min stimulation (pulse) provides a sufficient time frame for the uptake of Atto647N nanobodies in the recycling pool of SVs (Gaffield and Betz, 2006). The neurons were then washed extensively with low K^+ buffer to remove unbound Atto647N nanobodies and incubated for 10 min in low K^+ buffer (chase). To detect Atto647N nanobodies trapped in single SVs, they were then partially bleached to discriminate single SVs in the highly crowded presynaptic environment, after which we acquired time-lapse videos (50 Hz) of single-molecule fluorescence datasets of Atto647N nanobodies (Video 1), which were used to obtain high-resolution mean intensity images (Fig. 1 D), diffusion coefficients (Fig. 1 E), and single-molecule trajectory maps (Fig. 1 F). To minimize the nonspecific background, we omitted analyzing single-molecule tracks shorter than eight time points. To visualize the confined (Fig. 1 G) and mobile (Fig. 1 H) fractions of SVs, the single-particle tracking data were filtered based on the diffusion coefficients. Internalized single molecules exhibited various mobility patterns (Fig. 1 I): single (i) or dual confinement (ii) and free diffusion (iii) and directed movement (iv). SVs were also observed to move in groups where multiple vesicles visited a confinement site (Fig. 1 I, v) or moved in a circular directed pattern at the perimeter of an active nerve terminal (Fig. 1 I, vi).

Mobility of VAMP2–pHluorin–bound Atto647N nanobodies decreases when internalized in SVs

To validate the sdTIM technique, we compared the mobility of VAMP2–pHluorin/Atto647N nanobodies on the plasma membrane with that of internalized nanobodies. For this, we used a technique called Universal Point Accumulation Imaging in Nanoscale Topography (uPAINT; Giannone et al., 2010, 2013), which is ideal to establish the mobility of plasma membrane proteins (Fig. S1 A) and has previously been used to track single glutamate receptors using anti-GFP nanobodies (Nair et al., 2013). Hippocampal neurons were transfected with VAMP2–pHluorin (Fig. S1 B) for 24 h and imaged at 50 Hz during high K^+ stimulation in the presence of Atto647N nanobodies. After single-particle tracking (Nair et al., 2013), we generated superresolved mean intensity images (Fig. S1 C), diffusion coefficients (Fig. S1 D), and single-molecule trajectory maps (Fig. S1 E) of VAMP2–pHluorin/Atto647N nanobodies on the plasma membrane.

We then compared the mobility of VAMP2 on the plasma membrane (uPAINT) with that of internalized VAMP2 (sdTIM) by calculating the MSD (μm^2) using the PALMtracer plug-in (Kechkar et al., 2013; Nair et al., 2013) for MetaMorph. As expected, we observed a significant reduction in the mobility of internalized VAMP2 compared with that on the plasma membrane (Fig. 2 A). The area under the MSD curve (AUC) for each cell in each condition also showed a significant decrease in mobility upon VAMP2 internalization (Fig. 2 B). We next analyzed the diffusion coefficient (D) of the single-molecule trajectories. Based on our observations, the frequency distribution of the $Log_{10}D$ values of VAMP2–pHluorin/Atto647N nanobodies on the plasma membrane and internalized in SVs was bimodal. The threshold for the immobile and mobile fractions (indicated by the dashed line in Fig. 2 C) was calculated as described

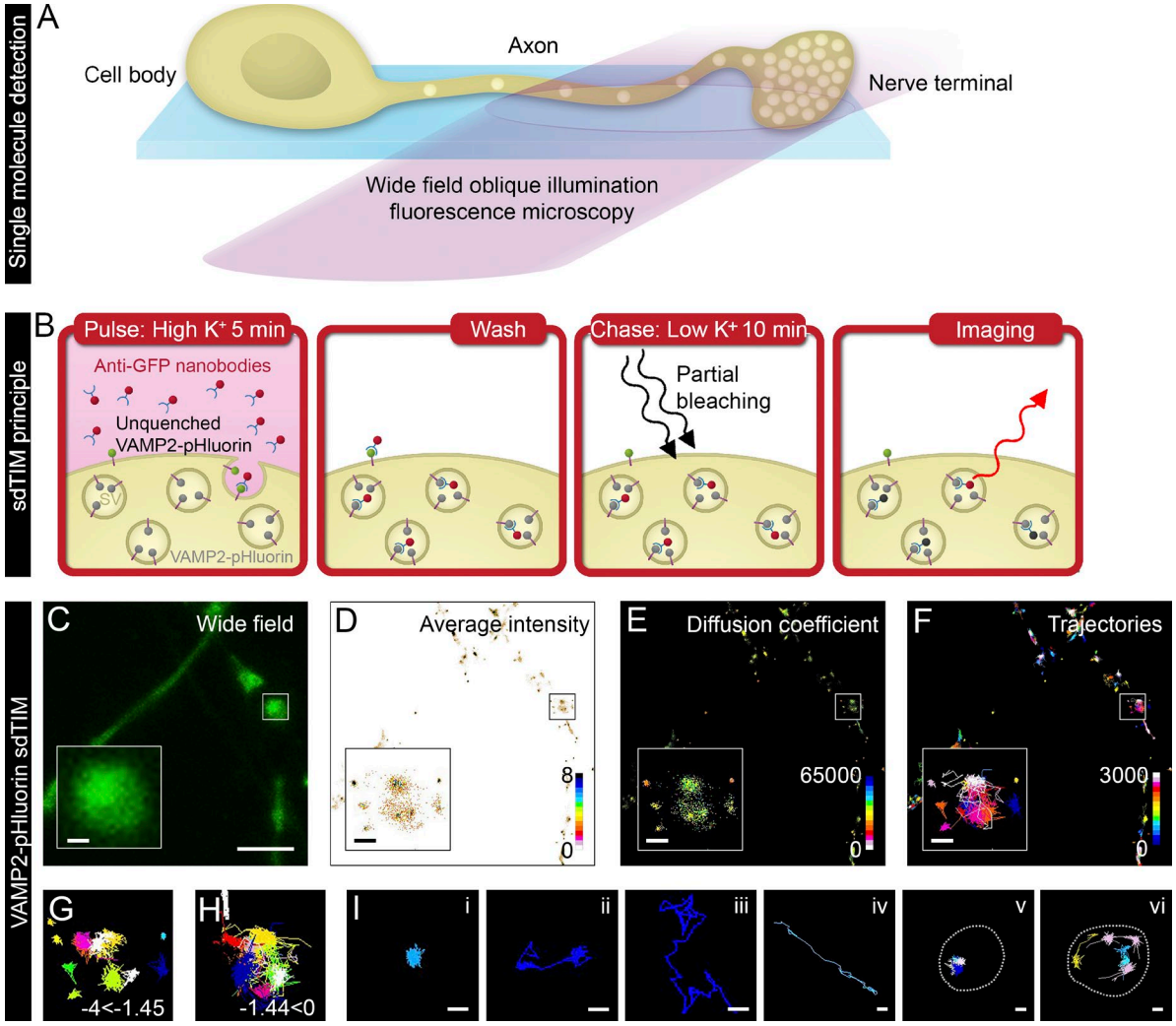

Figure 1. **sdTIM detects the internalized VAMP2–pHluorin–bound Atto647N nanobodies in SVs.** (A) Scheme of single fluorescent molecule detection in axons and nerve terminals using oblique illumination. (B) The sdTIM principle: hippocampal neurons expressing VAMP2–pHluorin were stimulated for 5 min with Atto647N nanobody–containing (red) high K^+ buffer. After stimulation, the excess nanobodies were washed off, and the neurons were chased for 10 min in low K^+ buffer. To detect nanobodies inside individual SVs, the nerve terminals were then exposed to intense laser illumination to bleach the majority of the Atto647N fluorophores, and a subset of internalized Atto647N fluorophores in SVs (red) could then be detected. (C) Wide-field image of hippocampal neuron expressing VAMP2–pHluorin subjected to sdTIM. (D) The corresponding superresolved mean intensity image shows the density map of VAMP2 localization from 3,643 trajectories. The colored bar represents localization densities, and the colder colors indicate higher density. (E) Diffusion coefficient image of VAMP2 localizations from 3,643 trajectories. The detection range from $Log_{10}D = -4$ to 0 and the warmer colors in the color scale indicate lower mobility. (F) Corresponding trajectories of the VAMP2 mobility over 3,000 frames. Trajectory color-coding refers to acquisition frame number. Boxed areas are shown with higher magnification. Confined ($-4 \leq Log_{10}D \leq -1.45$) (G) and unconfined ($-1.45 < Log_{10}D \leq 0$) (H) trajectories of the VAMP2–pHluorin–bound Atto647N nanobodies are shown from the boxed regions indicated in C–F. (I) Representative trajectories of single (i) and dual confinement (ii), free diffusion (iii), directed motion (iv), confined vesicular movement at a site revisited by several vesicles (v; presynapse outlined with dashed line for clarity), and circular movement at the perimeter of an active nerve terminal (vi; presynapse outlined with dashed line for clarity). Bars: (C) 5 µm; (C–F, insets) 0.5 µm; (I) 0.25 µm.

earlier (Constals et al., 2015): the displacement threshold was 0.03 $\mu m^2\ s^{-1}$ ($Log_{10}D = -1.45$, if $[D] = \mu m^2\ s^{-1}$). The immobile fraction was composed of VAMP2–pHluorin/Atto647N nanobodies for which displacement within four frames was below the spatial detection limit of our method (106 nm). Internalized VAMP2–pHluorin/Atto647N nanobodies displayed a significantly higher frequency of immobile molecules ($Log_{10}D \leq -1.45$) and a lower frequency of mobile molecules ($Log_{10}D > -1.45$) than those detected on the plasma membrane (Fig. 2 C and Fig. S2 A). Correspondingly, the mobile-to-immobile ratio of VAMP2–pHluorin/Atto647N nanobodies was significantly higher for molecules on the plasma membrane than for internalized molecules (Fig. 2 C, inset). The mobile-to-immobile ratio of internalized VAMP2–pHluorin/Atto647N nanobodies was similar to that reported earlier for other major SV proteins, synaptophysin– and synaptotagmin–pHluorin (Gimber et al., 2015), as well as for postsynaptic AMPA receptors (Groc et al., 2007), validating the use of VAMP2–pHluorin as an SV marker. The average diffusion coefficient for the mobile fraction of VAMP2–pHluorin on the plasma membrane was 0.14 $\mu m^2\ s^{-1}$, which is similar to that reported earlier for VAMP2–pHluorin (Gimber et al., 2015). The average diffusion coefficient for the immobile fraction of internalized VAMP2–pHluorin was 0.009 $\mu m^2\ s^{-1}$, which is similar to the mobility reported in a recent study on SV mobility in pools (Rothman et al., 2016). The localization precision (σ; Michalet, 2010) was 36.0 ± 1.6 nm

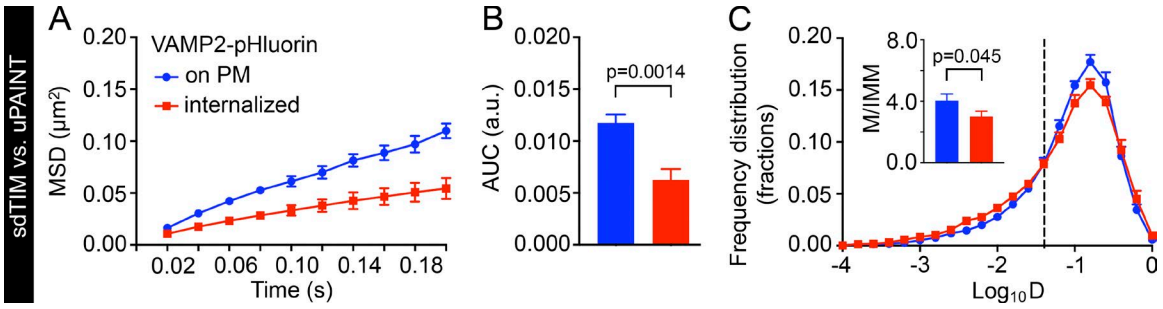

Figure 2. **Internalized VAMP2–pHluorin/Atto647N nanobodies exhibit lower mobility compared with those transiting on the plasma membrane.** Hippocampal neurons were transfected with VAMP2–pHluorin and subjected to sdTIM or uPAINT, and the mobility of VAMP2–pHluorin–bound Atto647N nanobody after internalization was compared with VAMP2–pHluorin/Atto647N nanobody mobility on the plasma membrane (PM). The graphs show MSD (A; μm^2), AUC (B; in arbitrary units [a.u.]), and frequency distribution (C) of the mean $Log_{10}D$. The threshold for the mobile ($Log_{10}D \leq -1.45$) and immobile fraction ($Log_{10}D > -1.45$) is indicated with a dashed line. The inset in C shows the mobile-to-immobile (M/IMM) ratios of VAMP2–pHluorin/Atto647N nanobodies internalized in SVs and transiting on the plasma membrane. $n = 12$ hippocampal neurons in individual cultures in sdTIM (97,400 trajectories) and uPAINT (52,800 trajectories). Statistical analyses of independent experiments were performed using the Student's *t* test (C, inset) and Mann–Whitney *U* test (B). Error bars are ±SEM. See also Fig. S2 A.

for uPAINT and 36.2 ± 1.3 nm for sdTIM, similar to the value reported previously for SV tracking (Westphal et al., 2008).

To further characterize the mobility of SVs and to account for nonlinear diffusion, we analyzed their MSS and compared the results of sdTIM experiments to uPAINT controls. Previously recorded movies were analyzed using the utrack program (Jaqaman et al., 2008). In contrast to MSD measurements, MSS (Ferrari et al., 2001; Ewers et al., 2005) allows examination of cases other than the second moment of moving particles (i.e., anomalous and subdiffusive events). The utrack program also allowed us to recover diffusion coefficients for each detected trajectory and plot the individual MSS slopes versus their respective diffusion coefficients. The distributions of the diffusion coefficient versus MSS slope values were significantly different for the sdTIM and the uPAINT experiments (Fig. S1 F). We also fitted the distributions to 2D Gaussian functions that further highlighted the different states and the shift toward smaller diffusion coefficient/MSS slope pairs for the sdTIM experiments (Fig. S1, G and H). These results demonstrate the presence of a distinct subset of VAMP2–pHluorin/Atto647N nanobody mobility in the sdTIM experiments, further validating that these trajectories are derived from Atto647N nanobodies internalized in SVs.

sdTIM enables simultaneous detection of multiple SVs in live hippocampal nerve terminals

Despite exhibiting some variability (Mutch et al., 2011), a mean of 70 copies of VAMP2 can be found in SVs (Wilhelm et al., 2014). Given this large number of VAMP2 copies per SV, there was a high probability of multiple nanobodies being trapped in a single SV, even when used at very low concentrations. The stochastic number of nanobodies per vesicle and the random number of Atto647N molecules per nanobody made it challenging to determine the number of vesicles for which movement was visualized in a crowded presynaptic terminal. To overcome this issue, we used single-molecule detection and stepwise photobleaching to calculate the number of conjugated Atto647N molecules per nanobody and the number of nanobodies in the presynaptic terminal. A low concentration of Atto647N nanobodies was deposited on a clean glass surface to minimize the chance of detecting two or more nanobodies within the same diffraction-limited spot. We then monitored the stepwise emission of fluorescence to directly assess the number of Atto647N molecules per nanobody. At a neutral pH, 28% of emission traces had one step, 36% showed two steps, and 28% had three steps (Fig. 3, A and B). A small number of traces (8%) had more than three steps, which is consistent with a random distribution of the protein on the glass surface. When we monitored the fluorescence emission of Atto647N nanobodies at pH 5.0 to mimic the low intravesicular pH (Mel'nik et al., 1985; Fig. 3 C), no change in the average number of Atto647N emission steps per nanobody was detected (Fig. 3 D). However, we noticed a slight increase in the signal to noise ratio of individual emission steps in the intensity-time traces. The fluorescence stability of Atto647N allowed us to reliably count more than five emission steps (example trace in Fig. S2 B).

In our sdTIM experiments, hippocampal neurons were exposed to partial bleaching so that single moving vesicles could be followed. The number of bleaching steps helped us to determine the number of vesicles in the nerve terminals. This was achieved by imaging fixed neurons after uptake of Atto647N nanobodies (sdTIM). The bleaching time, before imaging, was adjusted to maximize the detection of single step emission from single SVs in presynapses. This ensured that most of the fluorophores were bleached and that the large majority of SVs contained only one nanobody, with only one or two emitting Atto647N fluorophores. Representative fluorescence-time traces obtained from synaptic regions in fixed hippocampal neurons are shown in Fig. 3 E, together with the distribution of Atto647N nanobody emission steps after the initial bleaching (Fig. 3 F). The average number of emission steps originating from a single SV was 1.5.

In live hippocampal neurons, internalized Atto647N nanobodies could easily be traced after a similar initial bleaching step before imaging in sdTIM. We detected single SVs entering the presynaptic nerve terminals, followed by their confined motion within this region and exit into the perisynaptic region. To determine the number of SVs that resided within the active zone at any given time, two methods were used. First, to obtain intensity-time traces, we recorded the fluorescence intensity of each detected spot within the single particle trajectories. The fluorescence of the trajectories did not change as long as only one vesicle was followed in the presynaptic region. When a second vesicle entered the region and was found within the same diffraction-limited spot, a steplike increase in fluorescence was

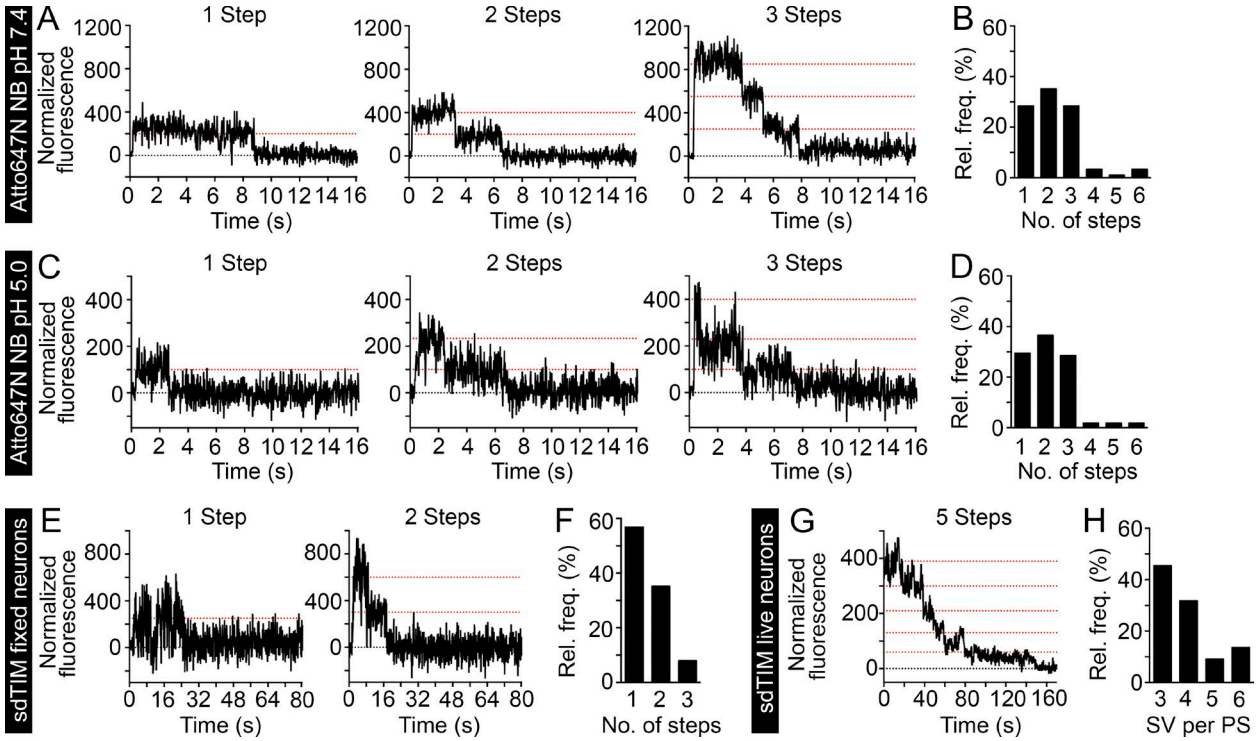

Figure 3. **sdTIM enables the simultaneous detection of multiple SVs in live hippocampal nerve endings.** Highly diluted Atto647N nanobodies were deposited on a glass surface, and the fluorescence emission was recorded over time. (A and B) At pH 7.4 (n = 90 Atto647N nanobodies), 28% of traces show one, 36% show two, and 28% show three steps. (C and D) At pH 5.0 (n = 106 Atto647N nanobodies), 29% of traces show one, 37% show two, and 29% show three steps. At both pHs, a small number of traces (<8%) showed more than three steps, as a consequence of more than one antibody being found within the same diffraction-limited spot. The graphs in B and D show the relative frequencies of the detected emission steps. To estimate the number of fluorophores per SV, hippocampal neurons expressing VAMP2–pHluorin were subjected to sdTIM, as described in Fig. 1, and fixed. Representative one- and two-step fluorescence time (s) traces obtained from fixed presynapses are shown (E) together with the relative frequency (%) of Atto647N emission steps after bleaching (F). Note that in the majority of cases, the SVs exhibited only one fluorescence step, with an average ratio of Atto647N fluorophores per nanobody of 1.5:1. (G) After sdTIM, a representative fluorescence-time trace from a live hippocampal neuron presynapse is shown. (H) Relative frequency of detected SVs in live presynaptic terminals. Dotted red lines in the graphs indicate the detected emission steps. n = 88 traces from 22 presynapses originating from five neurons.

observed. We counted the total number of emission steps from all trajectories recovered from one nerve terminal to estimate the maximum number of vesicles for which positions could be detected within the same diffraction-limited spot. The average number of steps was 5.4 ± 1.3 (SD). In the second approach, a region of interest was chosen to cover the whole presynaptic terminal. The fluorescence intensity over time exhibited similar step-like emission to that in fixed cells, with the number of steps reflecting the number of nanobodies within that region (Fig. 3 G). We found a mean of 6.0 ± 1.6 (SD) steps, which was in good agreement with the results from the first method. Given that after bleaching there was on average, 1.5 fluorescently active Atto647N molecules per nanobody and estimating one nanobody per vesicle, we calculated that the number of SVs we could detect within each presynaptic active zone, at any given time, was 4 ± 1 (Fig. 3 H). These results highlight the potential of simultaneous detection of several SVs in the crowded environment of the hippocampal presynapse.

SV movement in active presynapses is highly confined

The assessment of SV mobility in nerve terminals has previously been based on morphological features of the neuron (Rizzoli and Betz, 2004). To unequivocally discriminate active nerve terminals from surrounding axonal segments, VAMP2–pHluorin fluorescence (Fig. 4, A and B) was imaged during high K^+ stimulation and concomitant uptake of Atto647N nanobodies. As expected, after SV fusion and VAMP2–pHluorin unquenching, the fluorescence intensity increased significantly in presynaptic sites compared with axons (Fig. 4, C and D), as previously established (Gimber et al., 2015). Nerve terminals (Fig. 4, E and F) and intersynaptic axonal segments (Fig. 4, E and I) were then partially bleached (Fig. 4, G and J) and imaged at 50 Hz to detect internalized Atto647N nanobodies. Single-molecule tracking of Atto647N nanobodies trapped in SVs in active presynapses was achieved by delineating regions that exhibited activity-dependent fluorescence unquenching. The mobility of internalized Atto647N nanobodies in presynapses was mostly confined (Fig. 4 H), with more mobile tracks being found in axonal segments (Fig. 4 K). As previously established, we could detect SVs moving in and out of active presynapses (Fig. 4 H, dark blue track); this most likely reflects intersynaptic vesicle exchange (Kamin et al., 2010), a process that has been proposed to be involved in synaptic homeostasis and plasticity in vivo (Herzog et al., 2011).

SVs were significantly less mobile in active presynapses than in axons, as demonstrated by comparing the MSD curves and AUC of VAMP2–pHluorin/Atto647N nanobodies in the respective regions (Fig. 4, L and M, respectively). Accordingly, the $Log_{10}D$ showed a significantly larger immobile fraction of

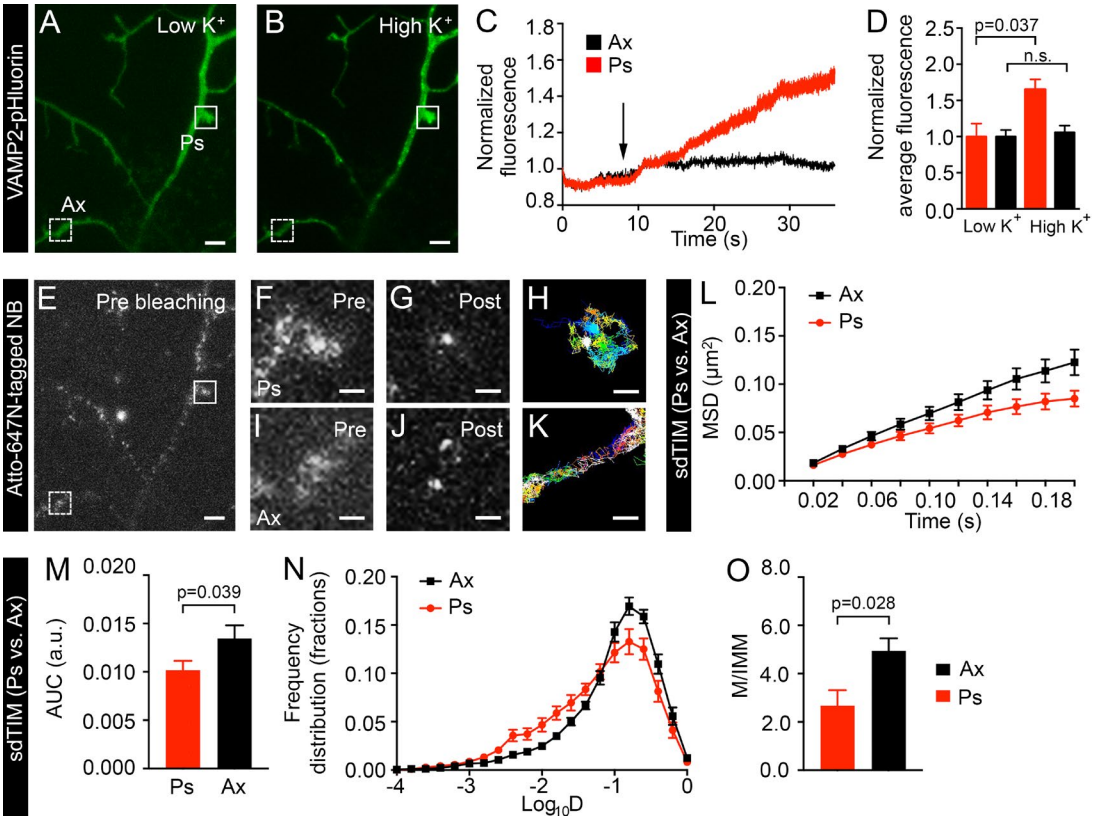

Figure 4. **Mobility of internalized VAMP2 differs in presynapses and axons.** To identify active nerve terminals, hippocampal neurons expressing VAMP2–pHluorin were incubated in low K^+ buffer (A) followed by 5-min stimulation in high K^+ buffer (B). (C) Fluorescence intensity of VAMP2–pHluorin as a function of time (s) in the axonal segment (Ax) and presynapse (Ps; dashed-line and continuous-line box indicated in A, respectively). The arrow indicates the time point for high K^+ stimulation. (D) Normalized mean intensity of VAMP2–pHluorin at axons and presynapses in low K^+ and high K^+. n = 20 presynapses and 20 axonal segments from five neurons in individual cultures. Values in C and D were normalized to the first acquired frame. (E) Fluorescence image of internalized Atto647N nanobodies (NB) in the same hippocampal neuron shown in A and B. Corresponding presynapse and axonal segment from A are indicated with a continuous- and dashed-line box, respectively, and shown with higher magnification before (Pre) and after bleaching (Post) in F and G and I and J, respectively. The trajectories from the corresponding regions of the presynapse (H) and axonal segment (K) are shown. Bars: (A, B, and E) 5 µm; (F–K) 1 µm. The mean MSD (L; μm^2), AUC (M; arbitrary units [a.u.]), mean frequency distribution of $Log_{10}D$ (N), and the mobile-to-immobile (M/IMM) fraction (O) of SVs in presynapses and axonal segments obtained from sdTIM experiments. n = 113 presynapses (27,700 trajectories) and 80 axonal segments (21,200 trajectories) from 12 hippocampal neurons in individual cultures. Statistical analyses of independent experiments were performed using the Student's t test (D and O) or Mann–Whitney U test (M). Error bars are ±SEM. See also Fig. S2 C.

SVs in presynapses compared with axons (Fig. 4 N and Fig. S2 C). Consequently, we detected a significantly smaller mobile-to-immobile ratio in presynapses than in axons (Fig. 4 O). These results are in good agreement with previous studies performed by SV immunolabeling (Kamin et al., 2010) using QuantumDot-based presynaptic probes (Lee et al., 2012) or surface-resident VAMP2–pHluorin (Sankaranarayanan and Ryan, 2000). Our results confirm that intersynaptic SV mobility (which occurs in axons) is greater than in presynapses. To analyze the mobility of internalized VAMP2–pHluorin/Atto647N nanobodies in live hippocampal neurons (Fig. S3 A) in more detail, we calculated the vector displacement for each SV trajectory and the cumulative magnitude of these vectors in 100-nm^2 grids to obtain a quiver plot of the detected single molecules (Fig. S3 B). The resulting vector map clearly exhibited areas of vector convergence and lower displacement consistent with the expected SV confinement in presynapses (Fig. S3 C) as compared with axonal regions (Fig. S3 D).

To confirm the correct targeting of the Atto647N nanobodies in SVs, hippocampal neurons were subjected to sdTIM, fixed, and immunostained against another SV protein, Synapsin-1. As expected, the unquenched signal of VAMP2–pHluorin in active presynapses after stimulation colocalized with labeling against endogenous Synapsin-1 (Fig. 5 A), confirming the identity of the active presynapses. Importantly, we only detected Atto647N nanobodies internalized in neurons expressing VAMP2–pHluorin (Fig. 5, B and C), confirming the anti-GFP specificity of the nanobodies (Kubala et al., 2010). To assess the correct localization of the nanobodies in SVs, we performed correlative light microscopy and EM. Hippocampal neurons were grown on gridded cell culture dishes and transfected with VAMP2–pHluorin for 24 h, after which the localization of the neurons expressing VAMP2–pHluorin on the grids was recorded (Fig. 5 D). Cells were then processed for sdTIM except for the use of anti-GFP HRP-mCherry-GFP nanotrap (GNT) nanobodies and omitting the live-cell imaging of the SVs. After internalization, the neurons were fixed, subjected to cytochemical staining, and processed for EM. The VAMP2–pHluorin–positive neurons were then located based on their recorded position on the grids. This allowed us to identify the precise localization of the nanobodies in these neurons based on the electron-dense precipitate produced by the HRP substrate (Fig. 5 E). Although some of the HRP precipitate was detected in endocytic structures >45 nm in diameter, the great majority

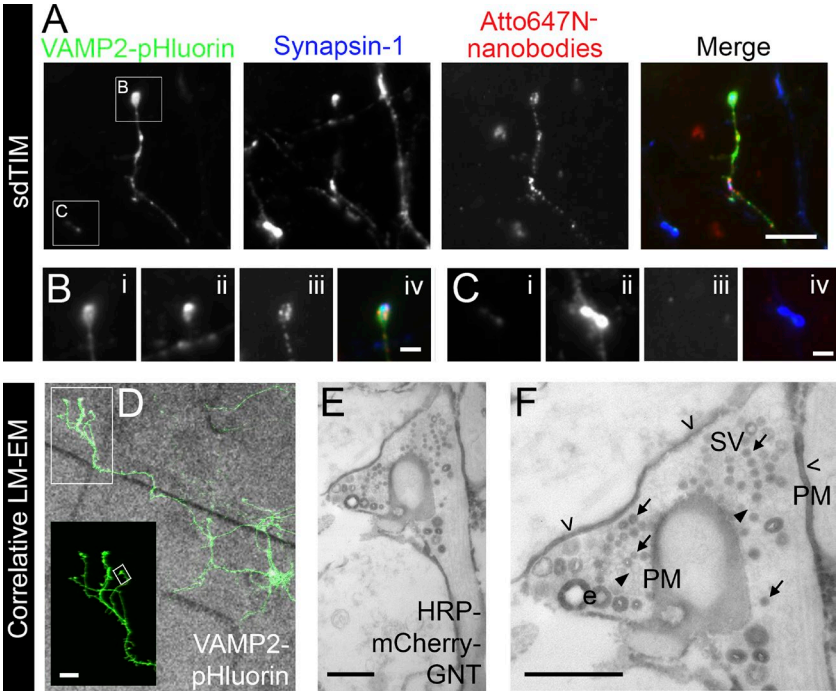

Figure 5. **Localization of internalized anti-GFP nanobodies in VAMP2–pHluorin–expressing hippocampal neurons.** (A) Hippocampal neurons expressing VAMP2–pHluorin were subjected to sdTIM, fixed, and immunolabeled against endogenous Synapsin-1 (pseudocolored in blue). The merged image shows an overlay of the images. Bar, 5 µm. The boxed areas are shown with higher magnification in B and C. Bars, 1 µm. (B) VAMP2–pHluorin (i) colocalized with Synapsin-1 (ii) in active presynapses containing VAMP2–pHluorin–bound Atto647N nanobodies (iii), as seen in the merged image (iv). (C) Presynapses positive for Synapsin-1 (ii), but not for VAMP2–pHluorin (i), did not contain Atto647N nanobodies (iii), as shown in the merged image (iv). Hippocampal neurons were grown on gridded glass-bottom dishes and transfected with VAMP2–pHluorin. (D) The localization of live VAMP2–pHluorin–positive neurons on the grids was recorded, and the cells were then subjected to sdTIM using HRP-mCherry-GNT. After fixation and cytochemical staining, the neurons were processed for EM. VAMP2–pHluorin expression is shown at higher magnification in the inset from the indicated boxed area. Bar, 10 µm. (E) The same neuron was then located in the electron micrograph by following the recorded location of the cells on the grid. (F) HRP precipitate in SVs (arrows), residual staining (open arrowheads) on the plasma membrane (PM), unstained vesicles (arrowheads), and bulk endosomes (e) are indicated. The presynapse shown in E and F is indicated with the tilted box in D. Bars, 0.5 µm. LM-EM, light microscopy and EM.

(88.5 ± 3.0%) was found in SVs (Fig. 5 F). We also observed some residual staining on the plasma membrane, indicating that not all nanobodies were internalized. Importantly, the neurons not expressing VAMP2–pHluorin did not contain internalized HRP precipitate. These results provide validation of the specific internalization of the GFP-bound nanobodies into SVs at VAMP2–pHluorin–positive nerve terminals and further validate the use of sdTIM to track SVs in active presynapses.

Restimulation increases presynaptic SV mobility

Neurotransmission is mediated by SV exocytosis at presynapses. Although considerable efforts have been dedicated to studying the events leading to SV exocytosis (Betz et al., 1992; Lemke and Klingauf, 2005; Kamin et al., 2010), the details of how SVs move toward the plasma membrane to undergo fusion (Kamin et al., 2010) remain unclear.

In agreement with a previous study demonstrating that recently endocytosed SVs are more mobile and become gradually less mobile when integrated into vesicle clusters (Kamin et al., 2010), our MSD measurements of the recently endocytosed SVs (t_0–t_{120s}) compared with resting SVs (t_0–t_{200s}) indicated a significant decrease in mobility over time (Fig. S4, A–C). To study the dynamic steps leading to exocytosis and neurotransmitter release, we introduced a second round of high K^+ stimulation (restimulation) of live VAMP2–pHluorin–expressing hippocampal neurons after the initial uptake of Atto647N nanobodies and compared the mobility with the corresponding time frame of the sdTIM (t_0–t_{120s}). Restimulation with high K^+ after the internalization of Atto647N nanobodies led to the unquenching of VAMP2–pHluorin and an increase in fluorescence similar to that detected during the first round of stimulation (Fig. 6, A–C), thereby confirming the localization of functional release sites. Restimulation increased the SV mobility significantly when compared with unstimulated conditions in both whole neurons (Fig. 6, D–F; and Fig. S2 D) and presynaptic regions of interest (Fig. 6, G–I; and Fig. S2 E). Interestingly, the restimulation had no effect on the mobility of intersynaptic SVs (Fig. 6, J–L) imaged in axonal segments. These results are different from those of a previous study that showed that stimulation had no effect on the mobility of recently endocytosed SVs (Kamin et al., 2010). However, the authors could only assess SV mobility minutes after the stimulus, suggesting that they may have missed effects at the onset or offset of stimulation. The discrepancy in results might therefore be explained by our ability to follow the restimulation effects on SV mobility immediately after introduction of the second stimulus with high K^+ (within 10 s).

When comparing the effects of restimulation on SV mobility between axons and presynapses, we observed similar, although less profound, differences in the MSD and $Log_{10}D$ measurements (Fig. 7, A–C; and Fig. S2 F) than in our previous sdTIM results (Fig. 4, L–O), with SVs being more mobile in axons than in presynapses. Based on our earlier observations, the mobility of SVs increased upon restimulation in presynapses (Fig. 6, G–I; and Fig. S2 E) but remained unaltered in axons (Fig. 6, J–L). Interestingly, although the SV mobility increased in presynapses, it did not rise to the level observed in axons (Fig. 7, A–C; and Fig. S2 F). Together, these results indicate that the mechanisms responsible for the SV mobility detected in axons are most likely different from those in presynapses.

Interestingly, our data demonstrate that the increase in SV mobility elicited by restimulation is indistinguishable from that of VAMP2–pHluorin–bound Atto647N nanobodies on the plasma membrane (Fig. 7, D–F). These results indicate that, upon restimulation, SVs relocate to the plasma membrane and undergo exocytosis, after which the SV contents, including VAMP2–pHluorin–bound Atto647N nanobodies, are released to move on the plasma membrane. These results are consistent

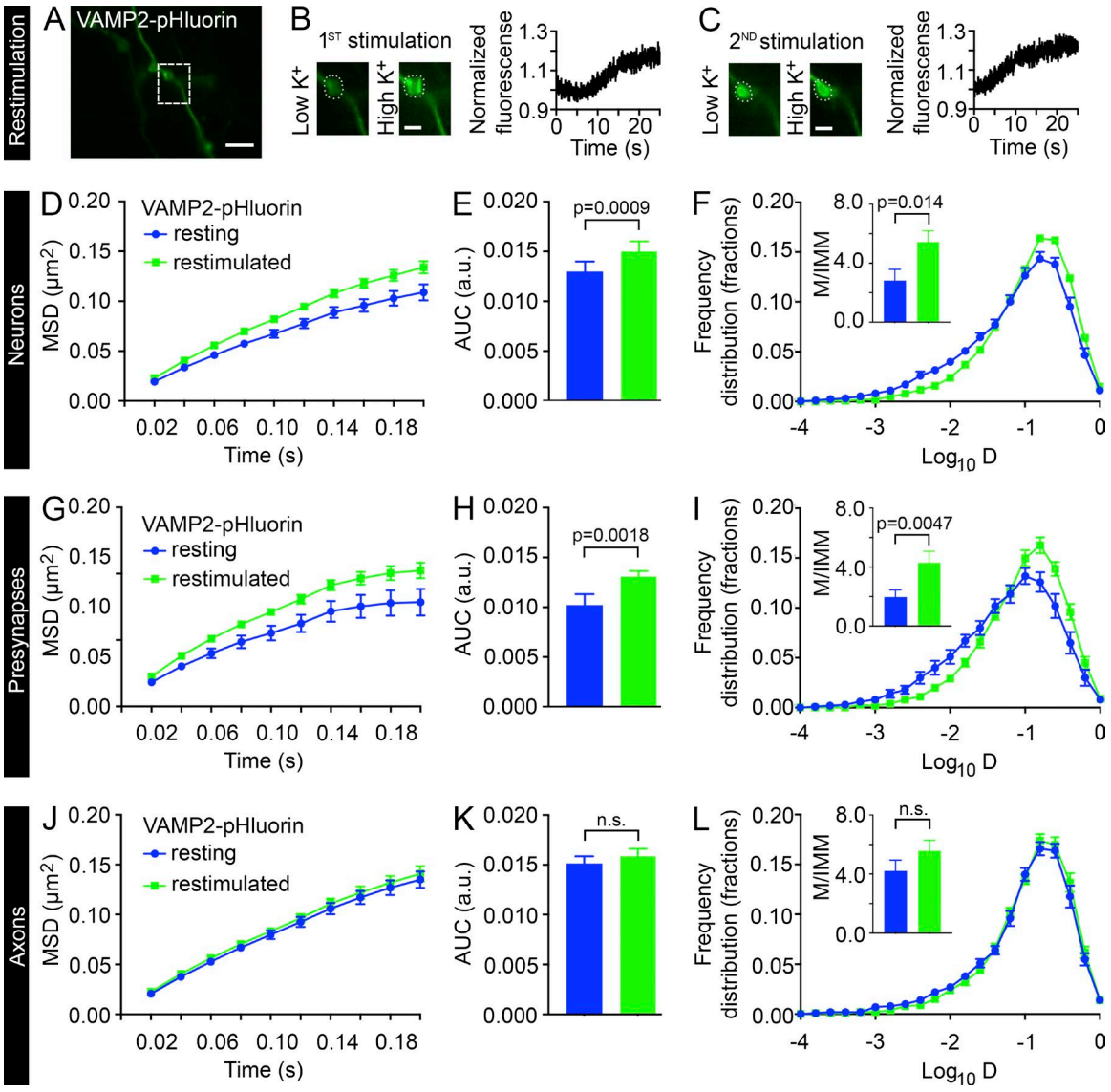

Figure 6. **Restimulation increases the mobility of internalized VAMP2 in presynapses but not in axons.** (A) Hippocampal neurons expressing VAMP2–pHluorin were subjected to sdTIM. After the first 5-min high K^+ stimulation (B) and 10-min chase, the neurons were subjected to a second stimulation (restimulation) with high K^+ (C), and the fluorescence of VAMP2–pHluorin was recorded. The boxed presynapse in A is shown at higher magnification before and after the first (B) and second (C) stimulation. The corresponding fluorescence intensity of VAMP2–pHluorin during the first and second high K^+ stimulation is shown in B and C, respectively. The intensities were normalized to the first acquired frame. Bars: (A) 5 µm; (B and C) 2 µm. (D–L) The SV mobility in resting and restimulated neurons subjected to sdTIM was compared in neuronal, presynaptic, and axonal regions of interest. The mean MSD (D, G, and J; μm^2), AUC (E, H, and K; arbitrary units [a.u.]), and mean frequency distribution of $Log_{10}D$ and the M/IMM fraction (F, I, and L) after restimulation from indicated regions. $n_{internalized}$ = 17 hippocampal neurons (45,200 trajectories) and $n_{restimulated}$ = 23 neurons (33,000 trajectories) (D–F), $n_{internalized}$ = 74 presynapses from 17 hippocampal neurons (13,600 trajectories) and $n_{restimulated}$ = 113 presynapses from 23 hippocampal neurons (7,800 trajectories) (G–I), and $n_{internalized}$ = 108 axonal segments from 17 hippocampal neurons (23,600 trajectories) and $n_{restimulated}$ = 148 axonal segments from 23 hippocampal neurons (21,500 trajectories) (J–L), all in individual cultures. Statistical analyses of independent experiments were performed using the Student's *t* test (F, I, and L, insets) or Mann–Whitney *U* test (E, H, and K). Error bars are ±SEM. See also Fig. S2 (D and E).

with those of a previous study showing that the mobility of vesicular proteins increases after their translocation to the plasma membrane (Kamin et al., 2010). Together, our results suggest that the VAMP2–pHluorin/Atto647N nanobody mobility detected after restimulation contained information about the SV mobility inside presynapses and the dynamic events of exocytosis. Dissecting the exact time points of these events will provide a wealth of information regarding these crucial events and should prove an interesting subject for future studies. Furthermore, these results indicate that the sdTIM technique can be used to study the mobility of SVs after restimulation and, upon fusion, to investigate the dynamics of the VAMP2–pHluorin/Atto647N nanobodies on the plasma membrane. In contrast, although the mobility of single molecules on the plasma membrane can be addressed using styryl dyes, the dye repartitions into the extracellular solution shortly after exocytosis (Zenisek et al., 2002; Richards et al., 2005).

SVs stochastically switch between distinct motion states in presynapses and axons

Single-molecule trajectories are classically characterized using MSD and diffusion coefficient analyses (Gimber et al., 2015;

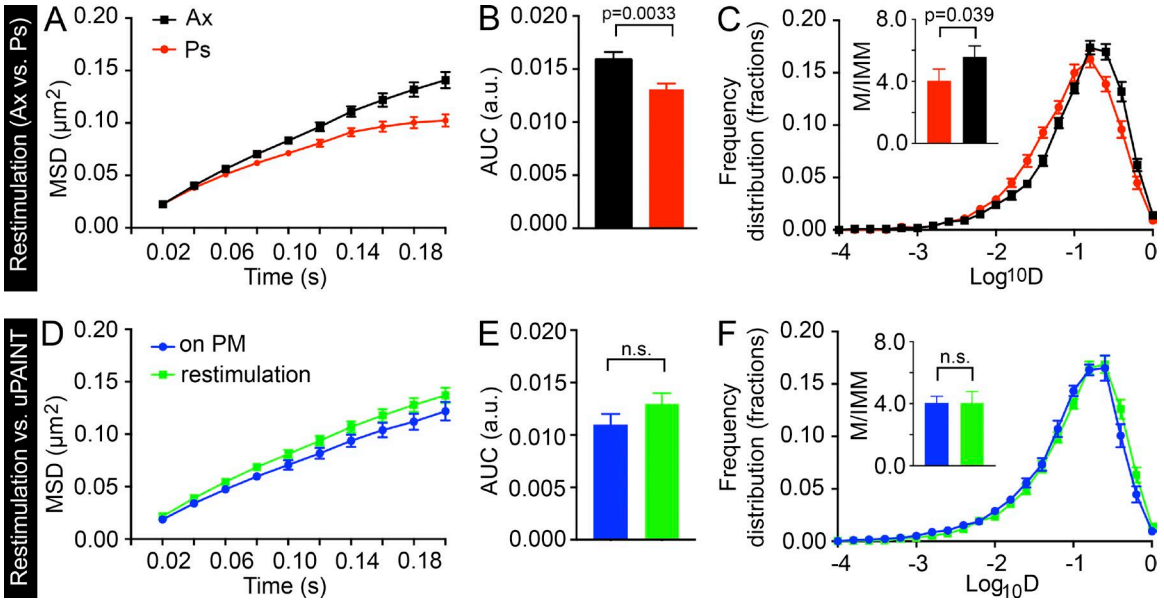

Figure 7. **Restimulation increases the SV mobility in presynapses to that of VAMP2–pHluorin mobility on the plasma membrane.** The mean MSD (A; μm²), AUC (B; arbitrary units [a.u.]), and mean frequency distribution of $Log_{10}D$ and the mobile-to-immobile (M/IMM) fraction (C) after restimulation in axonal segments (Ax) and presynapses (Ps). *n* = 113 presynapses and 148 axonal segments from 23 hippocampal neurons in individual cultures (7,800 and 21,500 trajectories, respectively). (D–F) Comparison of VAMP2–pHluorin/Atto647 nanobody mobility after restimulation to that detected on the plasma membrane (measured with uPAINT) in presynapses. Imaging was restricted to 120 s in both conditions. n_{uPAINT} = 50 presynapses from 12 hippocampal neurons (6,400 trajectories) and $n_{restimulation}$ = 113 presynapses from 23 hippocampal neurons (7,800 trajectories) in individual cultures. Statistical analyses of independent experiments were performed using the Student's *t* test (C and F, insets) or Mann–Whitney *U* test (B and E). Error bars are ±SEM. See also Fig. S2 F.

Maschi and Klyachko, 2015; Wang et al., 2015). The main disadvantage of these approaches is the time averaging, which results in loss of the alternating motion states along a single trajectory. HMMs have been successfully used to infer the number of motion states and the state transition probabilities from experimental data and to annotate each step of the trajectories with the respective motion state (Monnier et al., 2015). By using Bayesian model selection in the inference process, the simplest mobility model describing a set of trajectories can then be selected in an objective manner (Persson et al., 2013).

We therefore applied Bayesian model selection to HMMs to investigate the heterogeneous mobility patterns of internalized VAMP2–pHluorin/Atto647N nanobodies in live hippocampal neurons (see Materials and methods). It is common practice to analyze single-particle trajectories with a fixed number of hidden states (Das et al., 2009, 2015; Chung et al., 2010; Thurner et al., 2014; Freeman et al., 2015; Katz et al., 2016). When we assumed a maximum of four hidden states, we found that the optimal number of states was three for almost all presynapses (86%). Thus, for simplicity, we therefore assumed a maximum of three hidden states in our analysis. We observed heterogeneous transport dynamics across presynapses and axons. In 30 out of 31 presynapses and 28 out of 29 axonal segments, we detected three motion states, with the rest displaying two states. In both presynapses and axons, the mobility states displaying transport motion (65 and 93%, respectively) were more common than purely diffusive states (35 and 7%, respectively; Fig. 8 A). In 26% of the presynapses and 83% of the axonal segments, one state exhibited pure diffusive motion (D) with a low apparent diffusion coefficient (0.06 ± 0.01 and 0.06 ± 0.02 $\mu m^2\ s^{-1}$ on average in presynapses and axons, respectively) representing the immobile subpopulation, and the other two were active transport states (DV).

The angle between the velocity vectors of the two transport states in these D-DV-DV mobility states was close to 180° (173.7 ± 4.1°), indicating bidirectional movement. Interestingly, we found that the SVs underwent stochastic switching between these states (Fig. 8 B) and that the transition probabilities between the states differed (Fig. 8 C). In 32% of the presynapses, all three states were purely diffusive, with average apparent diffusion coefficients of 0.03 ± 0.01, 0.11 ± 0.01, and 0.32 ± 0.01 $\mu m^2\ s^{-1}$ (Fig. 8 D). The values for the other motion model types are given in Table S1.

In addition, our analysis provided population distributions of SV motion parameters in presynapses and axons (Fig. 8, E–G). In agreement with our earlier results (Fig. 4 L), we found that the average velocity of transport states (Fig. 8 F) was significantly higher ($P < 0.0001$) in axons (5.1 $\mu m\ s^{-1}$) than in presynapses (1.9 $\mu m\ s^{-1}$). These results are in agreement with a previous study (Shtrahman et al., 2005) showing that recycling SVs switch between bound and unbound states and spend more time in the immobile state. Furthermore, based on our results, the probability of remaining in the same state was higher for the diffusive state than the transport state in both presynapses and axons (Fig. 8 G), indicating that once an SV entered a diffusive state, it was relatively more likely to stay in that state than change to a transport state.

We next applied Bayesian model selection to HMMs for the restimulation data collected earlier. In 24 out of 34 presynapses and 32 out of 34 axonal segments, we detected three motion states, with the rest displaying two states. In both presynapses and axons, the mobility states displaying transport (74 and 97%, respectively) were more common than purely diffusive states (26 and 3%, respectively) (Fig. 9 A). The values for the other motion model are given in Table S1. The population distributions of SV motion parameters in presynapses and

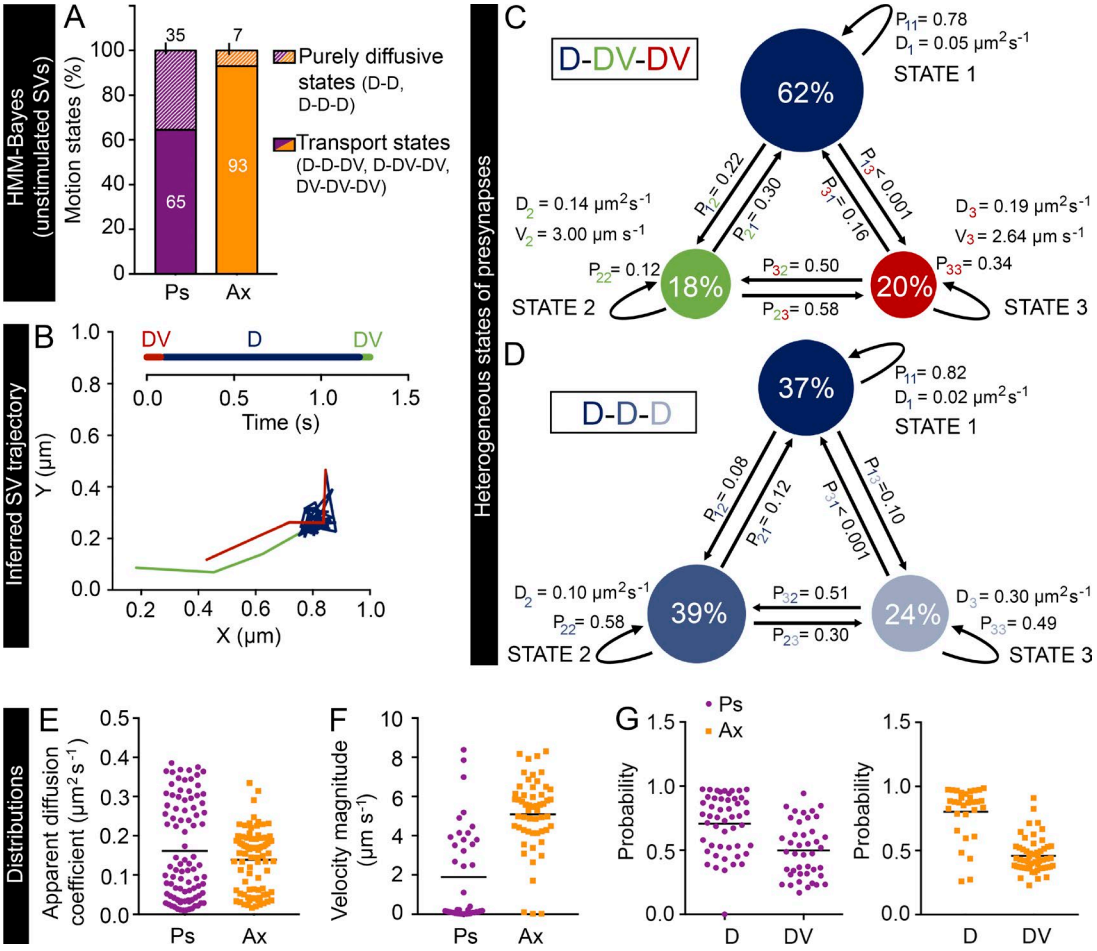

Figure 8. **HMM-Bayes analysis of the internalized VAMP2 in presynapses and axonal segments.** (A) Frequency of purely diffusive motion or a combination of diffusive and transport motion in presynapses (Ps) and axons (Ax). D indicates a diffusive state, and DV indicates a transport state. (B) An example SV trajectory displaying D-DV-DV motion inferred by HMM-Bayes analysis. The timeline shows the order and duration of the motion states in the trajectory. (C and D) Examples of three-state D-DV-DV and D-D-D models in two presynapses, inferred from a set of VAMP2–pHluorin–bound Atto647N nanobody trajectories. Circles represent the different states, and their area is proportional to the percentage occupation of VAMP2–pHluorin–bound Atto647N nanobodies in the respective state. P_{ij}, where i = 1, 2, or 3 and j = 1, 2, or 3, are the transition probabilities, with i = j indicating the probability of staying in the same state and i ≠ j indicating the probability of switching to another state. The models in C and D also indicate the apparent diffusion coefficients (D) and velocity magnitudes (V) for the different states. The apparent diffusion coefficient distributions (E), the velocity magnitude distributions (F), and the probability of remaining in the same state in the next time step from all mobility states (G), including both diffusive and transport states, in axons and presynapses. In E–G, the horizontal line indicates the mean. *n* = 31 presynapses (12,000 trajectories) and 29 axonal segments (16,700 trajectories) from seven and six hippocampal neurons, respectively, in individual cultures.

axons are shown in Fig. 9 (B–D). The average velocity magnitude of SVs was significantly higher ($P < 0.0001$) in axons than in presynapses (5.0 and 3.3 μm s^{-1}, respectively). These results reveal that synaptic vesicles are actively transported within presynapses rather than relying on passive diffusion alone, as suggested by previous studies (Holt et al., 2004; Rea et al., 2004; Tokuoka and Goda, 2006; LoGiudice et al., 2008; Rothman et al., 2016). HMM-Bayes model selection applied to SVs in presynapses and axons demonstrated both a heterogeneous combination of diffusive and transport states and stochastic switching between these states.

Discussion

Single-particle tracking allows the characterization of the mobility of a single protein and can provide unprecedented insights into the motion heterogeneities associated with crucial cellular events (Freeman et al., 2016). Most insights regarding SV mobility have been gained by indirect methods, such as fluorescence recovery after photobleaching (Henkel and Betz, 1996; Kraszewski et al., 1996; Gaffield et al., 2006; Rothman et al., 2016) and correlation spectroscopy (Jordan et al., 2005; Shtrahman et al., 2005; Yeung et al., 2007). Other approaches have used a variety of styryl dyes to study endosomal trafficking in general (Lemke and Klingauf, 2005; Gaffield and Betz, 2006; Peng et al., 2012) or viral delivery (Gandhi and Stevens, 2003) to accomplish sparse labeling of SVs and the subsequent tracking of a relatively low number of SVs per presynapse. A hallmark study in the field provided high-resolution imaging of isolated vesicles in live hippocampal terminals and throughout the entire axons using stimulated emission depletion microscopy (Westphal et al., 2008).

Commonly, only two diffusive states of SV mobility (bound and free) are assumed, and single-particle tracking data have been fitted based on this assumption (Bakshi et al.,

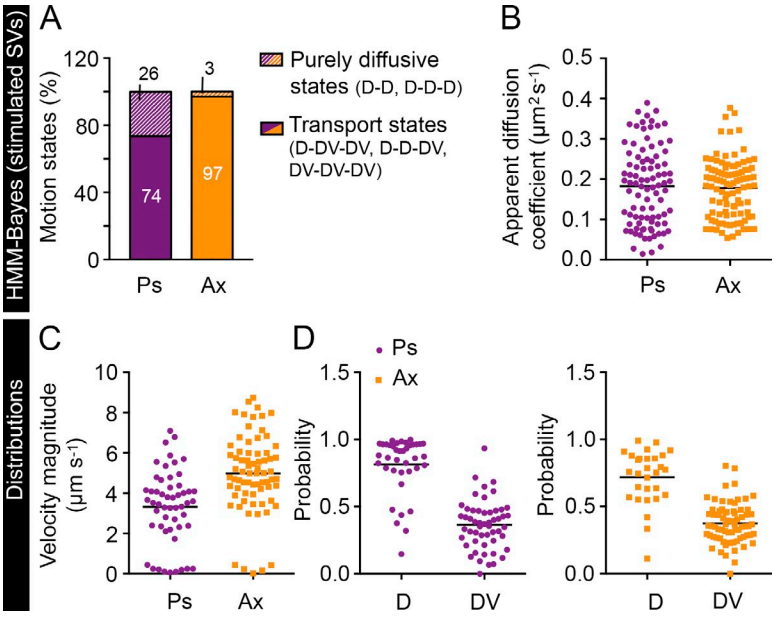

Figure 9. **HMM-Bayes analysis of the restimulation effects on the VAMP2 mobility.** (A) Percentage of presynapses (Ps) and axons (Ax) exhibiting purely diffusive motion (D) or a combination of diffusive and transport motion (DV). The apparent diffusion coefficient distributions (B), the velocity magnitude distributions (C), and the probability of remaining in the same state in the next time step from all mobility states (D), including both diffusive and transport states, in axons and presynapses. n = 34 presynapses (7,000 trajectories) and 34 axonal segments (12,300 trajectories) from 15 and 12 hippocampal neurons, respectively, in individual cultures. In B–D, the horizontal line indicates the mean.

2012). Most current single-particle tracking techniques, such as the ones using photoconvertible fusion proteins, generate large numbers of relatively short trajectories, demonstrating the need for methods that can track and analyze a large number of trajectories simultaneously over longer periods (Manley et al., 2008; Persson et al., 2013). Several other techniques have previously been used to characterize SV mobility (Lemke and Klingauf, 2005; Westphal et al., 2008; Hoopmann et al., 2010; Kamin et al., 2010; Hua et al., 2011; Gimber et al., 2015). The main advantage of the sdTIM technique compared with these methods is that it takes advantage of several technological advances, such as the use of smaller nanobodies conjugated with stable Atto647-fluorophores with increased fluorescence lifetime, which are ideal for superresolution microscopy. This allowed us to follow several SVs simultaneously for longer timeframes. Furthermore, sdTIM is a relatively fast and simple technique with a high spatiotemporal resolution (36-nm localization precision and 20-ms imaging rate), and is capable of generating high-density output data. Monitoring pHluorin fluorescence during nanobody loading or unloading has allowed us to be highly confident that the trajectories we retrieved stemmed from either nerve terminals or axonal segments. The resulting high-density output data enabled us, in turn, not only to determine the average diffusion but also to isolate the heterogeneous stages of the individual SVs, providing novel insights into SV mobility in live hippocampal neurons. One of the major advantages of sdTIM is that it is also likely to prove valuable in the context of genetic or pharmacological manipulations.

The internalization of Atto647N nanobodies was only detected in VAMP2–pHluorin–positive neurons, indicating a selective endocytic uptake in SVs, a result that was confirmed by correlative light microscopy and EM. It is worth noting, however, that upon pulse-chase uptake of VAMP2–pHluorin–bound Atto647N nabobodies, we also detected a fraction of molecules that retained the same mobility as that of molecules detected on the plasma membrane with uPAINT (Gordon et al., 2011), as well as a residual HRP precipitate on the plasma membrane and in endosomes in the electron micrographs. Although the diffusion coefficient threshold between mobile and immobile fractions has been previously used as a criterion to identify the plasma membrane-resident population from internalized SVs (Lee et al., 2012), our results reveal a remarkable heterogeneity in SV mobility, even along a single trajectory. We therefore cannot exclude the possibility that a small fraction of our single-molecule detections originate from structures other than SVs. Although providing a powerful tool to study SV mobility, sdTIM uses oblique illumination and is therefore limited to imaging a thin optical section. Furthermore, our tracking is performed in 2D, and further advances in the field such as the use of astigmatic lenses will be required to assess the mobility of single molecules in 3D. Moreover, although sdTIM can be used to study the mobility steps of SV recycling, it cannot be used to detect all pools of SVs at the simultaneously. The use of dual fluorescence imaging should address this limitation.

Tracking single vesicles revealed mobile and immobile fractions that exhibited various mobility patterns and confinement. Directed movement at the perimeter of presynapses suggests that cytoskeletal elements could be involved in driving active motion. Another nonexclusive possibility is that the directed motion of a vesicle or other organelle could generate nanofluidic effects capable of mobilizing a trail of freely moving SVs before their recruitment. Such behavior is compatible with previous findings indicating that decreased mobility of SVs results from their incorporation into vesicle clusters and docking sites (Kamin et al., 2010) and that vesicle collisions and hydrodynamic interactions are among the major determinants of SV mobility in crowded presynaptic terminals (Rothman et al., 2016). Our data showed that the mobility of internalized VAMP2–pHluorin/Atto647N nanobodies was significantly lower in active nerve terminals than on the plasma membrane. Furthermore, our results demonstrating that the internalized VAMP2–pHluorin/Atto647N nanobody mobility decreased gradually and was significantly lower than that found in axonal segments are in good agreement with previous studies (Westphal et al., 2008; Kamin et al., 2010). Restimulation reversed these effects in the presynapse, but not in the axonal segments. Ultimately, the SVs resumed mobility that was indistinguishable from that of VAMP2–pHluorin/Atto647N nanobodies on the plasma membrane, indicating that upon SV exocytosis, these nanobodies could be detected transiting on

the plasma membrane. Dissecting the precise temporal nature of these highly dynamic SV recycling events will allow further investigations of the key steps of SV mobility during neurotransmission. Although these questions remain to be addressed in future studies, our results validate the power of the sdTIM technique for the study of the entire SV cycle.

The HMM-Bayes analysis allowed us to unveil a range of apparent diffusion coefficients for SVs in presynapses. When averaged, the values obtained were consistent with those of some earlier studies (Holt et al., 2004; Rea et al., 2004) but differed from those of other studies (Jordan et al., 2005; Lemke and Klingauf, 2005; Shtrahman et al., 2005; Gaffield and Betz, 2006). One of the features of sdTIM is that this method is capable for producing hundreds of trajectories for each presynapse and thousands for each neuron. This allowed us to identify a wide range of apparent diffusion coefficients without the caveat inherent in time averaging, which leads to the loss of hidden mobility states and state transitions. The commonly presented average values therefore do not accurately represent the fluctuations in SV mobility. Furthermore, the use of different markers, cell types, methods, and time scales in the experiments might also lead to differing results. Finally, it is important to stress that the values reported in our study were not corrected for localization precision and motion blur and therefore only present apparent diffusion coefficients.

By applying the HMM-Bayes analysis to single-molecule data, we have provided a comprehensive analysis of the heterogeneous motion states of SVs in presynapses and axons in resting and stimulated neurons. In contrast to the current view, our results revealed a stochastic switching between the diffusive and transport motion of SVs. Our analysis also showed that SVs are relatively less likely to switch from diffusive states to transport states in either resting or stimulated neurons. It is noteworthy that the main conclusion from this analysis, that SVs stochastically switch between different motion states, does not depend on the maximum number of hidden states allowed. The sdTIM technique described in this study can potentially be applied to study other subdiffractional endocytic structures, enabling measurements of changes in SV mobility in response to genetic or pharmacological manipulations. Although further experiments will be required to address the mechanisms underlying these diverse diffusive states and transport dynamics, our study provides the first quantitative account of the heterogeneous nature of SV mobility.

Materials and methods

Neuronal cultures

Hippocampal neurons were obtained from Sprague Dawley rats at embryonic day 18 as previously described (Kaech and Banker, 2006; Heine et al., 2008; Harper et al., 2011) and cultured on poly-D-lysine–coated glass-bottom dishes (D29-20-1.5N; Cellvis) at 50,000–100,000 cell densities. Experiments were conducted with the approval of The University of Queensland Animal Ethics Committee. Neurons were transfected with Lipofectamine 2000 (11668–019; Invitrogen) at 14–17 DIV, according to the manufacturer's protocol, and imaged at 15–18 DIV.

Constructs and antibodies

VAMP2–pHluorin was provided by J. Rothman (Yale University, New Haven, CT; Miesenböck et al., 1998). The primary Synapsin-1 antibody (106011; Synaptic Systems) and the secondary antibody Alexa Fluor 564 (A11030; Invitrogen) were obtained from the respective manufacturers. The anti-GFP nanobody (gift from K. Alexandrov, Institute for Molecular Bioscience, The University of Queensland, Brisbane, Australia) was labeled with Atto647N according to the manufacturer's protocol (ATTO-TEC GmbH) as previously described (Harper et al., 2016). Nanobodies were diluted to 1 mg ml^{-1} and dialyzed against 20:1 PBS, pH 7.4/0.2 M $NaHCO_3$, pH 9.0. A two- to threefold molar excess of Atto-647N normal human serum–ester, which was reconstituted in DMSO, was then added to the solution of nanobodies and incubated at room temperature for 1 h. Excess dye was removed using a Sephadex gel filtration column (17-0851-01; GE Healthcare), and a Bradford protein assay (B6916; Sigma-Aldrich) was performed to determine the concentration of the labeled protein. HRP-mCherry-GNT was constructed as follows: a prokaryotic mCherry-GNT expression vector yielding N-terminal fusion of the 6His-Ubiquitin tag (Catanzariti et al., 2004) was constructed using circular polymerase extension cloning (Quan and Tian, 2011). In brief, mCherry (Takara Bio Inc.) and GNT (Kirchhofer et al., 2010) were inserted into the pHUE backbone, using a set of appropriate primers (pHUE forward: 5′-AGCTTAGATCCGGCT GCTAACAAAGCCCG-3′; and pHUE reverse: 5′-TCCACCGCGGAG GCGCAACACCAGGTGCAG-3′; mCherry forward: 5′-TGTTGC GCCTCCGCGGTGGA*TGC*AGCAGCGGTGTGAGCAAGGGCGA-3′; and mCherry reverse: 5′-CCGCTTTCCACCAGTTGAACCTGC ATCTTGTACAGCTCGTCCATGCCGCCGGT-3′; and GNT forward: 5′-ATGCAGGTTCAACTGGTGGAAAGCGG-3′; and GNT reverse: 5′-CGGGCTTTGTTAGCAGCCGGATCTAAGCTTCAAGAGCTCA CCGTCACCTGAGTCCCCTG-3′). Sequences encoding a cysteine residue (indicated in italics) were introduced between the ubiquitin tag and mCherry. The engineered cysteine was exposed to the N-terminal of the mCherry-GNT fragment because of proteolytic cleavage using deubiquitylating enzymes (Catanzariti et al., 2004). The cysteine residue appended to an N-terminal extension of the mCherry-GNT protein was reduced to free sulfhydryl with mercaptoethylamine hydrochloride (2-MEA; Thermo Fisher Scientific) at a concentration of 20 mM in PBS at room temperature for 1 h. Reduced protein was separated from excess reducing agent by gel filtration over a desalting gel (PD-10; GE Healthcare). The protein was eluted with ice-cold PBS, concentrated to 5 mg ml^{-1}, and then applied for labeling. Peroxidase maleimide activated (P1709; Sigma-Aldrich) was reconstituted to 5 mg in ice-cold PBS and then combined with mCherry-GNT in a 1:2 ratio. The reaction mixture was incubated at 4°C with gentle agitation overnight. After reaction, the unreacted free HRP and mCherry-GNT were separated using gel filtration chromatography (Superdex-75; GE Healthcare).

Reagents

Hepes (H3375), ascorbic acid (A5960), $CaCl_2$ (C5080), and BSA (A8022) were purchased from Sigma-Aldrich. $NaCl_2$ (X190) and D-glucose (0188) were purchased from AMRESCO. KCl (1206119; Ajax Finechem Pty Limited) and $MgCl_2$ (MA029; Chem-Supply) were purchased from the respective manufacturers.

sdTIM

Cultured hippocampal neurons expressing VAMP2–pHluorin were washed once with a low K^+ buffer (0.5 mM $MgCl_2$, 2.2 mM $CaCl_2$, 5.6 mM KCl, 145 mM NaCl, 5.6 mM D-glucose, 0.5 mM ascorbic acid, 0.1% BSA, and 15 mM Hepes, pH 7.4), after which the neurons were incubated with high K^+ buffer (as in low K^+ with the exception of 95 mM NaCl and 56 mM KCl) containing 3.19 pg μl^{-1} Atto647N-tagged nanobodies for 5 min at 37°C. After stimulation, unbound Atto647N nanobodies were washed off with low K^+ buffer, and neurons were then chased for 10 min at 37°C to maximize the internalization of VAMP2–pHluorin–bound Atto647N-tagged nanobodies.

To detect single molecules of the internalized nanobodies, the nerve terminals were exposed to high laser illumination to partially bleach the majority of the Atto647N fluorophores, and the remaining internalized Atto647N nanobodies were imaged using oblique illumination microscopy. Localization precision, σ (36.2 ± 1.3 nm), was calculated according to $\varepsilon = 4\sigma^2$ (Michalet, 2010), where ε is the y-intercept of the average of the MSD values.

uPAINT

Experiments were performed as per Giannone et al. (2010). Hippocampal neurons from rats were transfected with VAMP2–pHluorin. To track VAMP2–pHluorin, we used anti-GFP Atto647N nanobodies (Kubala et al., 2010) at 3.19 pg μl^{-1} concentration. σ (36.0 ± 1.6 nm) was calculated as described in the sdTIM section.

Oblique illumination microscopy

For live-cell oblique illumination, neurons were visualized at 50-Hz (10,000–20,000 frames by image streaming) and 20-ms exposure, at 37°C on a microscope equipped with an ILas^2 double-laser illuminator (Roper Technologies), a CFI Apo TIRF 100× 1.49 NA objective (Nikon), and an Evolve512 delta EMCCD camera (Photometrics). Image acquisition was performed using Metamorph software (MetaMorph Microscopy Automation and Image Analysis Software, version 7.7.8; Molecular Devices). A quadruple beam splitter (LF 405/488/561/635-A-000-ZHE; Semrock) and a QUAD band emitter (FF01-446/510/581/703-25; Semrock) were used.

Single-molecule detection and tracking

The single-molecule localization and dynamics were extracted from the 6,000–10,000 frame oblique illumination acquisitions as described earlier (Nair et al., 2013). The VAMP2–pHluorin–bound Atto647N-tagged nanobodies were detected and tracked using a combination of wavelet segmentation (Izeddin et al., 2012) and optimization of multi-frame object correspondence by simulated annealing (Racine et al., 2006). PALM-Tracer, a custom-written program that runs as a plug-in within the Metamorph software, was used for molecule localization and tracking of the VAMP2 dynamics (MSD and diffusion coefficient, D). The $Log_{10}D$ distribution was sorted into immobile and mobile fractions as previously described (Constals et al., 2015). We only included tracks longer than eight frames in the analysis to minimize nonspecific background. The color coding for the superresolved images was performed using ImageJ (2.0.0-rc-43/1.50e; National Institutes of Health). Diffusion coefficients were calculated for each trajectory and presented in a color-coded pixel at the site of localization. In the mean intensity maps, each pixel indicates an individual molecule. The area with the highest density is represented in black, whereas white represents regions with no detection. The color-coding of the trajectory maps represents the detection time point along the acquisition: cold colors indicate early detections.

Nanobody fluorescence intensity fluctuation analysis

Single Atto647N-conjugated nanobodies were imaged in a 22 × 10 × 1-mm chamber, the bottom of which was made of microscope coverglass (Menzel Glaser, 1.5; Thermo Fisher Scientific). Before assembling the chamber, the cover glass was cleaned by sonication for 20 min in 1 M KOH, followed by extensive rinsing in Milli-Q water (EMD Millipore) and drying by airflow. 200-µl of nanobodies diluted in PBS ($1:10^4$) were incubated in the chamber for 15 min before washing with PBS only. For experiments in an acidic environment, PBS was titrated with hydrochloric acid until it reached pH 5.0 and then used immediately. The density of nanobodies was 50–100 per 27 × 27 μm^2. For the characterization of nanobodies, 5 × 5 pixels around the center of each fluorescent spot were chosen to obtain intensity-time traces using a custom-written routine described previously (Durisic et al., 2014). The background was subtracted locally and calculated from the mean intensity of the region two pixels larger than the edge of the Atto647N nanobody signal. Partially overlapping nanobodies and fluorophores that photobleached in less than two frames were excluded from the analysis. Emission steps were counted manually and defined as events in which the mean intensity of the smallest step was at least twice the SD of the background fluorescence. The steps within each single trace were similar in amplitude. Missed events were found in <2% of traces, and an appropriate correction was made. It was imperative that the signal-to-noise ratio was at least 1.5 so that the number of counted steps accurately reflected the number of fluorophores. Intensity-time traces from synaptic regions were extracted and characterized in the same way, except that the region of interest was adjusted to cover the whole synapse. The average number of steps in presynaptic vesicles was 6.0 (±1.6 SD). Given that the ratio of Atto647N fluorophore dyes per nanobody was 1.5:1 and assuming one Atto647N nanobody per vesicle, we estimate that we were able to detect, on average, 4 ± 1 labeled SVs in the presynapse at any given time.

Correlative light and EM

Rat hippocampal neurons (embryonic day 18) were grown on gridded glass-bottom dishes (P35G-1.5-14-CGRD-D; MatTek Corporation) and transfected with VAMP2–pHluorin on 14–16 DIV. On 15–17 DIV, the neurons were imaged live at 37°C on an inverted point-scanning laser confocal microscope (ZIS LMS 510 META; ZEISS), with a Plan-APO 10× 0.45 NA objective (ZEISS) using Zen 2009 software and an argon laser, to record the location of VAMP2–pHluorin–positive neurons on the cover grids. Neurons were then processed as described in the sdTIM section, with the exception of using anti-GFP HRP-mCherry-GNT and omitting single-particle imaging of SVs, and then fixed with 2.5% glutaraldehyde in PBS for 1 h at room temperature. After fixation, neurons were processed for DAB cytochemistry using standard protocols. Fixed cells were contrasted with 1% osmium tetroxide and 4% uranyl acetate before dehydration and embedded in LX-112 resin (Harper et al., 2011). Ultrathin sections (∼60 nm) were cut using an ultramicrotome (UC6FCS; Leica Biosystems). Neurons corresponding to those identified by fluorescence microscopy were visualized on a transmission electron microscope (model 1011; JEOL USA, Inc.) equipped with a cooled charge-coupled device camera (Morada; Olympus). The percentage of HRP-positive (cytochemically stained) SVs versus endocytic structures >45 nm in diameter was calculated from correlated electron micrographs of 25 VAMP2–pHluorin–expressing hippocampal neurons.

Vector quiver plot

To analyze the mobility of internalized VAMP2 in presynapses and axonal areas, previously recorded videos of sdTIM were analyzed with a custom python Qt5 GUI-based application called TrackerApp, which is available online as open-source software at https://github.com/QBI-Software/Tracking. The 2D displacement of each particle was used to calculate the polar coordinates for each trajectory. The xy coordinates of each particle position were then used to calculate the cumulative magnitude of the vectors in 100-nm^2 grids, as presented in the quiver plot, generated in the open source python library at matplotlib (http://matplotlib.org; based on MATLAB; MathWorks, Inc.). The vector plot is presented as arrows on a 2D Cartesian plane with reference to the point of origin at t_0.

Restimulation

After the pulse and chase uptake of VAMP2–pHluorin–bound Atto647N nanobodies, hippocampal neurons were restimulated with high

K^+, and the mobility of internalized Atto647N nanobodies was recorded immediately. To detect the release sites, we followed the unquenching of VAMP2–pHluorin upon restimulation as described earlier. We compared the mobility of restimulated SVs to resting SVs (sdTIM) by collecting 6,000 frames at 50 Hz in both conditions using the imaging setup described earlier. We estimate a 10-s delay in imaging after the second addition of high K^+.

MSS

To obtain trajectories and the MSS, previously recorded videos of sdTIM and uPAINT were analyzed using utrack (Jaqaman et al., 2008). utrack uses Gaussian mixture models to detect particles with overlapping signals. The displacement of a particle is given by $\langle r^v \rangle \sim t^{\gamma v}$ and the MSS plot shows γv versus v. We only analyzed tracks that were at least eight frames in length and obtained MSS and diffusion data from these trajectories.

Applying Bayesian model selection to HMM

We marked regions of interest around the presynapses and axonal segment and analyzed the trajectories from each region of interest separately using HMM-Bayes software (Monnier et al., 2015). For comparison, we also allowed a maximum of 4 hidden states and analyzed 29 presynapses from sdTIM experiments. However, in the great majority of cases (86% of presynapses), we found three or less motion states and thus for simplicity present only the results assuming a maximum of three hidden states in Figs. 8 and 9. The sdTIM results contain quantification from presynapses and axons, which resulted in an average of 386 ± 69 and 576 ± 132 trajectories per region of interest, respectively. The corresponding numbers in restimulation analysis were 230 ± 20 and 372 ± 48, respectively. All of the analyses were performed using MATLAB (MathWorks, Inc.). The average angle between transport states was calculated from all D-DV-DV models in axons and presynapses. The apparent diffusion coefficients were not corrected for localization precision and motion blur.

Image analysis and processing

The brightness and contrast of fluorescence images were adjusted with Photoshop CC 2015.1.1 (Adobe Systems Inc.). Color scaling of trajectories and fluorescence intensity analysis of time-lapse videos were done using ImageJ (National Institutes of Health), and the change in fluorescence was normalized to the first value for each experiment. Presynapses were selected based on their punctate morphology and the increased VAMP2 fluorescence intensity upon high K^+ stimulation. Axonal areas were selected based on their morphology and the absence of fluorescence variations elicited by stimulation.

Statistical analysis

All of the frequency-distributed data were tested in bins using two-tailed (unequal variances) Student's *t* tests in Excel (Microsoft). We used the nonparametric Mann–Whitney *U* test for the AUC and the velocity magnitudes in the HMM-Bayes results and the Kolmogorov-Smirnoff test for cumulative frequency of $Log_{10}D$ Prism (both with Prism C for Mac OS X Version 6.0g or Version 7.0a; GraphPad Software). To compare the D/MSS distributions, a 2D Kolmogorov-Smirnoff test was performed using MATLAB (MathWorks, Inc.). The AUC and frequency distribution were calculated with Prism (GraphPad Software). Error bars are ±SEM for independent experiments unless otherwise stated. The level of significance was set to $P < 0.05$.

Online supplemental material

Fig. S1 describes the principle of uPAINT to track VAMP2–pHluorin–bound Atto647N nanobodies on the plasma membrane and shows the results of the MSS analysis comparing sdTIM with uPAINT methods. Fig. S2 shows the cumulative frequencies of VAMP2–pHluorin/Atto647N nanobody mobility and an example of a six-step Atto647N nanobody emission curve. Fig. S3 shows the vector analysis. Fig. S4 shows the mobility differences of recently endocytosed SVs versus those at a later time point.

Acknowledgments

The superresolution microscopy was carried out at the Queensland Brain Institute's (QBI) Advanced Microimaging and Analysis Facility with the help of L. Hammond and R. Amor. We thank R. Martínez-Mármol (QBI) for help with the imaging, R. Gormal (QBI) for help with nanobody preparation, J. S. Borbely and M. Lakadamyali (Advanced Fluorescence Imaging and Biophysics group at The Institute of Photonic Sciences) for help with nanobody fluorescence intensity analysis, S. Manley, D. Choquet, J.-B. Sibarita, E. Hosy, and L. Cognet for insightful discussions, and R. Tweedale for critical appraisal of the manuscript.

This work was supported by an Australian Research Council Discovery Project grant (DP120104057) and an Australian Research Council Linkage Infrastructure, Equipment, and Facilities grant (LE130100078). F.A. Meunier is a Senior Research Fellow of the National Health and Medical Research Council and was the recipient of a Queensland International Fellowship. R.G. Parton is a Principal Research Fellow of the National Health and Medical Research Council and supported by National Health and Medical Research Council Program grant 1037320. P. Padmanabhan was supported by the University of Queensland Postdoctoral Research Fellowship.

The authors declare no competing financial interests.

Author contributions: M. Joensuu performed and analyzed the uPAINT and restimulation experiments. M. Joensuu and A. Papadopulos performed the sdTIM experiments. M. Joensuu analyzed the data, prepared the figures, and wrote the paper with P. Padmanabhan and F.A. Meunier. N. Durisic and M. Joensuu performed the nanobody fluorescence intensity fluctuation analysis. P. Padmanabhan, M. Joensuu, and A.T.D. Bademosi performed the Bayesian model selection to HMM, which was supervised by G.J. Goodhill. L. Cooper-Williams wrote the TrackerApp and designed the vector quiver plot analysis with A. Papadopulos. M. Joensuu and I.C. Morrow prepared the correlative EM samples. M. Joensuu, N. Durisic, and C. Harper prepared the Atto647N-tagged anti-GFP nanobodies. W. Jung prepared and characterized the peroxidase-labeled nanobodies, which was supervised by R.G. Parton. A. Papadopulos performed the MSS analysis and codesigned the study with F.A. Meunier. F.A. Meunier supervised the study.

Submitted: 1 April 2016
Accepted: 30 September 2016

References

Bakshi, S., A. Siryaporn, M. Goulian, and J.C. Weisshaar. 2012. Superresolution imaging of ribosomes and RNA polymerase in live *Escherichia coli* cells. *Mol. Microbiol.* 85:21–38. http://dx.doi.org/10.1111/j.1365-2958.2012.08081.x

Betz, W.J., G.S. Bewick, and R.M. Ridge. 1992. Intracellular movements of fluorescently labeled synaptic vesicles in frog motor nerve terminals during nerve stimulation. *Neuron.* 9:805–813. http://dx.doi.org/10.1016/0896-6273(92)90235-6

Catanzariti, A.M., T.A. Soboleva, D.A. Jans, P.G. Board, and R.T. Baker. 2004. An efficient system for high-level expression and easy purification of authentic recombinant proteins. *Protein Sci.* 13:1331–1339. http://dx.doi.org/10.1110/ps.04618904

Chung, I., R. Akita, R. Vandlen, D. Toomre, J. Schlessinger, and I. Mellman. 2010. Spatial control of EGF receptor activation by reversible dimerization on living cells. *Nature.* 464:783–787. http://dx.doi.org/10.1038/nature08827

Constals, A., A.C. Penn, B. Compans, E. Toulmé, A. Phillipat, S. Marais, N. Retailleau, A.S. Hafner, F. Coussen, E. Hosy, and D. Choquet. 2015. Glutamate-induced AMPA receptor desensitization increases their mobility and modulates short-term plasticity through unbinding from Stargazin. *Neuron.* 85:787–803. http://dx.doi.org/10.1016/j.neuron.2015.01.012

Couteaux, R., and M. Pécot-Dechavassine. 1974. Specialized areas of presynaptic membranes. [In French] *C. R. Acad. Sci. Hebd. Seances Acad. Sci. D.* 278:291–293.

Das, R., C.W. Cairo, and D. Coombs. 2009. A hidden Markov model for single particle tracks quantifies dynamic interactions between LFA-1 and the actin cytoskeleton. *PLOS Comput. Biol.* 5:e1000556. http://dx.doi.org/10.1371/journal.pcbi.1000556

Das, S., T. Yin, Q. Yang, J. Zhang, Y.I. Wu, and J. Yu. 2015. Single-molecule tracking of small GTPase Rac1 uncovers spatial regulation of membrane translocation and mechanism for polarized signaling. *Proc. Natl. Acad. Sci. USA.* 112:E267–E276. http://dx.doi.org/10.1073/pnas.1409667112

Durisic, N., L. Laparra-Cuervo, A. Sandoval-Álvarez, J.S. Borbely, and M. Lakadamyali. 2014. Single-molecule evaluation of fluorescent protein photoactivation efficiency using an in vivo nanotemplate. *Nat. Methods.* 11:156–162. http://dx.doi.org/10.1038/nmeth.2784

Ewers, H., A.E. Smith, I.F. Sbalzarini, H. Lilie, P. Koumoutsakos, and A. Helenius. 2005. Single-particle tracking of murine polyoma virus-like particles on live cells and artificial membranes. *Proc. Natl. Acad. Sci. USA.* 102:15110–15115. http://dx.doi.org/10.1073/pnas.0504407102

Ferrari, R., A.J. Manfroi, and W.R. Young. 2001. Strongly and weakly self-similar diffusion. *Physica D.* 154:111–137. http://dx.doi.org/10.1016/S0167-2789(01)00234-2

Freeman, S.A., V. Jaumouillé, K. Choi, B.E. Hsu, H.S. Wong, L. Abraham, M.L. Graves, D. Coombs, C.D. Roskelley, R. Das, et al. 2015. Toll-like receptor ligands sensitize B-cell receptor signalling by reducing actin-dependent spatial confinement of the receptor. *Nat. Commun.* 6:6168. http://dx.doi.org/10.1038/ncomms7168

Freeman, S.A., J. Goyette, W. Furuya, E.C. Woods, C.R. Bertozzi, W. Bergmeier, B. Hinz, P.A. van der Merwe, R. Das, and S. Grinstein. 2016. Integrins form an expanding diffusional barrier that coordinates phagocytosis. *Cell.* 164:128–140. http://dx.doi.org/10.1016/j.cell.2015.11.048

Gaffield, M.A., and W.J. Betz. 2006. Imaging synaptic vesicle exocytosis and endocytosis with FM dyes. *Nat. Protoc.* 1:2916–2921. http://dx.doi.org/10.1038/nprot.2006.476

Gaffield, M.A., S.O. Rizzoli, and W.J. Betz. 2006. Mobility of synaptic vesicles in different pools in resting and stimulated frog motor nerve terminals. *Neuron.* 51:317–325. http://dx.doi.org/10.1016/j.neuron.2006.06.031

Gandhi, S.P., and C.F. Stevens. 2003. Three modes of synaptic vesicular recycling revealed by single-vesicle imaging. *Nature.* 423:607–613. http://dx.doi.org/10.1038/nature01677

Giannone, G., E. Hosy, F. Levet, A. Constals, K. Schulze, A.I. Sobolevsky, M.P. Rosconi, E. Gouaux, R. Tampé, D. Choquet, and L. Cognet. 2010. Dynamic superresolution imaging of endogenous proteins on living cells at ultra-high density. *Biophys. J.* 99:1303–1310. http://dx.doi.org/10.1016/j.bpj.2010.06.005

Giannone, G., E. Hosy, J.B. Sibarita, D. Choquet, and L. Cognet. 2013. High-content super-resolution imaging of live cell by uPAINT. *Methods Mol. Biol.* 950:95–110. http://dx.doi.org/10.1007/978-1-62703-137-0_7

Gimber, N., G. Tadeus, T. Maritzen, J. Schmoranzer, and V. Haucke. 2015. Diffusional spread and confinement of newly exocytosed synaptic vesicle proteins. *Nat. Commun.* 6:8392. http://dx.doi.org/10.1038/ncomms9392

Gordon, S.L., R.E. Leube, and M.A. Cousin. 2011. Synaptophysin is required for synaptobrevin retrieval during synaptic vesicle endocytosis. *J. Neurosci.* 31:14032–14036. http://dx.doi.org/10.1523/JNEUROSCI.3162-11.2011

Groc, L., M. Lafourcade, M. Heine, M. Renner, V. Racine, J.B. Sibarita, B. Lounis, D. Choquet, and L. Cognet. 2007. Surface trafficking of neurotransmitter receptor: comparison between single-molecule/quantum dot strategies. *J. Neurosci.* 27:12433–12437. http://dx.doi.org/10.1523/JNEUROSCI.3349-07.2007

Harper, C.B., S. Martin, T.H. Nguyen, S.J. Daniels, N.A. Lavidis, M.R. Popoff, G. Hadzic, A. Mariana, N. Chau, A. McCluskey, et al. 2011. Dynamin inhibition blocks botulinum neurotoxin type A endocytosis in neurons and delays botulism. *J. Biol. Chem.* 286:35966–35976. http://dx.doi.org/10.1074/jbc.M111.283879

Harper, C.B., A. Papadopulos, S. Martin, D.R. Matthews, G.P. Morgan, T.H. Nguyen, T. Wang, D. Nair, D. Choquet, and F.A. Meunier. 2016. Botulinum neurotoxin type-A enters a non-recycling pool of synaptic vesicles. *Sci. Rep.* 6:19654. http://dx.doi.org/10.1038/srep19654

Heine, M., O. Thoumine, M. Mondin, B. Tessier, G. Giannone, and D. Choquet. 2008. Activity-independent and subunit-specific recruitment of functional AMPA receptors at neurexin/neuroligin contacts. *Proc. Natl. Acad. Sci. USA.* 105:20947–20952. http://dx.doi.org/10.1073/pnas.0804007106

Henkel, A.W., and W.J. Betz. 1996. Redistribution of clathrin and synaptophysin at the frog neuromuscular junction triggered by nerve stimulation: Immunocytochemical studies of vesicle trafficking. *Prog. Brain Res.* 109:41–46. http://dx.doi.org/10.1016/S0079-6123(08)62086-5

Herzog, E., F. Nadrigny, K. Silm, C. Biesemann, I. Helling, T. Bersot, H. Steffens, R. Schwartzmann, U.V. Nägerl, S. El Mestikawy, et al. 2011. In vivo imaging of intersynaptic vesicle exchange using VGLUT1 Venus knock-in mice. *J. Neurosci.* 31:15544–15559. http://dx.doi.org/10.1523/JNEUROSCI.2073-11.2011

Holt, M., A. Cooke, A. Neef, and L. Lagnado. 2004. High mobility of vesicles supports continuous exocytosis at a ribbon synapse. *Curr. Biol.* 14:173–183. http://dx.doi.org/10.1016/j.cub.2003.12.053

Hoopmann, P., A. Punge, S.V. Barysch, V. Westphal, J. Bückers, F. Opazo, I. Bethani, M.A. Lauterbach, S.W. Hell, and S.O. Rizzoli. 2010. Endosomal sorting of readily releasable synaptic vesicles. *Proc. Natl. Acad. Sci. USA.* 107:19055–19060. http://dx.doi.org/10.1073/pnas.1007037107

Hua, Y., R. Sinha, C.S. Thiel, R. Schmidt, J. Hüve, H. Martens, S.W. Hell, A. Egner, and J. Klingauf. 2011. A readily retrievable pool of synaptic vesicles. *Nat. Neurosci.* 14:833–839. http://dx.doi.org/10.1038/nn.2838

Izeddin, I., J. Boulanger, V. Racine, C.G. Specht, A. Kechkar, D. Nair, A. Triller, D. Choquet, M. Dahan, and J.B. Sibarita. 2012. Wavelet analysis for single molecule localization microscopy. *Opt. Express.* 20:2081–2095. http://dx.doi.org/10.1364/OE.20.002081

Jaqaman, K., D. Loerke, M. Mettlen, H. Kuwata, S. Grinstein, S.L. Schmid, and G. Danuser. 2008. Robust single-particle tracking in live-cell time-lapse sequences. *Nat. Methods.* 5:695–702. http://dx.doi.org/10.1038/nmeth.1237

Jordan, R., E.A. Lemke, and J. Klingauf. 2005. Visualization of synaptic vesicle movement in intact synaptic boutons using fluorescence fluctuation spectroscopy. *Biophys. J.* 89:2091–2102. http://dx.doi.org/10.1529/biophysj.105.061663

Kaech, S., and G. Banker. 2006. Culturing hippocampal neurons. *Nat. Protoc.* 1:2406–2415. http://dx.doi.org/10.1038/nprot.2006.356

Kamin, D., M.A. Lauterbach, V. Westphal, J. Keller, A. Schönle, S.W. Hell, and S.O. Rizzoli. 2010. High- and low-mobility stages in the synaptic vesicle cycle. *Biophys. J.* 99:675–684. http://dx.doi.org/10.1016/j.bpj.2010.04.054

Katz, Z.B., B.P. English, T. Lionnet, Y.J. Yoon, N. Monnier, B. Ovryn, M. Bathe, and R.H. Singer. 2016. Mapping translation 'hot-spots' in live cells by tracking single molecules of mRNA and ribosomes. *eLife.* 5:5. http://dx.doi.org/10.7554/eLife.10415

Kavalali, E.T., and E.M. Jorgensen. 2014. Visualizing presynaptic function. *Nat. Neurosci.* 17:10–16. http://dx.doi.org/10.1038/nn.3578

Kechkar, A., D. Nair, M. Heilemann, D. Choquet, and J.B. Sibarita. 2013. Real-time analysis and visualization for single-molecule based super-resolution microscopy. *PLoS One.* 8:e62918. http://dx.doi.org/10.1371/journal.pone.0062918

Kirchhofer, A., J. Helma, K. Schmidthals, C. Frauer, S. Cui, A. Karcher, M. Pellis, S. Muyldermans, C.S. Casas-Delucchi, M.C. Cardoso, et al. 2010. Modulation of protein properties in living cells using nanobodies. *Nat. Struct. Mol. Biol.* 17:133–138. http://dx.doi.org/10.1038/nsmb.1727

Kraszewski, K., L. Daniell, O. Mundigl, and P. De Camilli. 1996. Mobility of synaptic vesicles in nerve endings monitored by recovery from photobleaching of synaptic vesicle-associated fluorescence. *J. Neurosci.* 16:5905–5913.

Kubala, M.H., O. Kovtun, K. Alexandrov, and B.M. Collins. 2010. Structural and thermodynamic analysis of the GFP:GFP-nanobody complex. *Protein Sci.* 19:2389–2401. http://dx.doi.org/10.1002/pro.519

Lee, S., K.J. Jung, H.S. Jung, and S. Chang. 2012. Dynamics of multiple trafficking behaviors of individual synaptic vesicles revealed by quantum-dot based presynaptic probe. *PLoS One.* 7:e38045. http://dx.doi.org/10.1371/journal.pone.0038045

Lemke, E.A., and J. Klingauf. 2005. Single synaptic vesicle tracking in individual hippocampal boutons at rest and during synaptic activity. *J. Neurosci.* 25:11034–11044. http://dx.doi.org/10.1523/JNEUROSCI.2971-05.2005

Li, D., L. Shao, B.C. Chen, X. Zhang, M. Zhang, B. Moses, D.E. Milkie, J.R. Beach, J.A. Hammer III, M. Pasham, et al. 2015. Extended-resolution

structured illumination imaging of endocytic and cytoskeletal dynamics. *Science.* 349:aab3500. http://dx.doi.org/10.1126/science.aab3500

LoGiudice, L., P. Sterling, and G. Matthews. 2008. Mobility and turnover of vesicles at the synaptic ribbon. *J. Neurosci.* 28:3150–3158. http://dx.doi.org/10.1523/JNEUROSCI.5753-07.2008

Manley, S., J.M. Gillette, G.H. Patterson, H. Shroff, H.F. Hess, E. Betzig, and J. Lippincott-Schwartz. 2008. High-density mapping of single-molecule trajectories with photoactivated localization microscopy. *Nat. Methods.* 5:155–157. http://dx.doi.org/10.1038/nmeth.1176

Maschi, D., and V.A. Klyachko. 2015. A nanoscale resolution view on synaptic vesicle dynamics. *Synapse.* 69:256–267. http://dx.doi.org/10.1002/syn.21795

Mel'nik, V.I., R.N. Glebov, and G.N. Kryzhanovskiĭ. 1985. ATP-dependent proton translocation across the synaptic vesicle membrane in the brain of rats. [In Russian] *Biull. Eksp. Biol. Med.* 99:35–38.

Michalet, X. 2010. Mean square displacement analysis of single-particle trajectories with localization error: Brownian motion in an isotropic medium. *Phys. Rev. E Stat. Nonlin. Soft Matter Phys.* 82:041914. http://dx.doi.org/10.1103/PhysRevE.82.041914

Miesenböck, G., D.A. De Angelis, and J.E. Rothman. 1998. Visualizing secretion and synaptic transmission with pH-sensitive green fluorescent proteins. *Nature.* 394:192–195. http://dx.doi.org/10.1038/28190

Monnier, N., Z. Barry, H.Y. Park, K.C. Su, Z. Katz, B.P. English, A. Dey, K. Pan, I.M. Cheeseman, R.H. Singer, and M. Bathe. 2015. Inferring transient particle transport dynamics in live cells. *Nat. Methods.* 12:838–840. http://dx.doi.org/10.1038/nmeth.3483

Mutch, S.A., P. Kensel-Hammes, J.C. Gadd, B.S. Fujimoto, R.W. Allen, P.G. Schiro, R.M. Lorenz, C.L. Kuyper, J.S. Kuo, S.M. Bajjalieh, and D.T. Chiu. 2011. Protein quantification at the single vesicle level reveals that a subset of synaptic vesicle proteins are trafficked with high precision. *J. Neurosci.* 31:1461–1470. http://dx.doi.org/10.1523/JNEUROSCI.3805-10.2011

Nair, D., E. Hosy, J.D. Petersen, A. Constals, G. Giannone, D. Choquet, and J.B. Sibarita. 2013. Super-resolution imaging reveals that AMPA receptors inside synapses are dynamically organized in nanodomains regulated by PSD95. *J. Neurosci.* 33:13204–13224. http://dx.doi.org/10.1523/JNEUROSCI.2381-12.2013

Peng, A., Z. Rotman, P.Y. Deng, and V.A. Klyachko. 2012. Differential motion dynamics of synaptic vesicles undergoing spontaneous and activity-evoked endocytosis. *Neuron.* 73:1108–1115. http://dx.doi.org/10.1016/j.neuron.2012.01.023

Persson, F., M. Lindén, C. Unoson, and J. Elf. 2013. Extracting intracellular diffusive states and transition rates from single-molecule tracking data. *Nat. Methods.* 10:265–269. http://dx.doi.org/10.1038/nmeth.2367

Pyle, J.L., E.T. Kavalali, E.S. Piedras-Rentería, and R.W. Tsien. 2000. Rapid reuse of readily releasable pool vesicles at hippocampal synapses. *Neuron.* 28:221–231. http://dx.doi.org/10.1016/S0896-6273(00)00098-2

Quan, J., and J. Tian. 2011. Circular polymerase extension cloning for high-throughput cloning of complex and combinatorial DNA libraries. *Nat. Protoc.* 6:242–251. http://dx.doi.org/10.1038/nprot.2010.181

Racine, V., A. Hertzog, J. Jouanneau, J. Salamero, C. Kervrann, and J.B. Sibarita. 2006. Multiple-target tracking of 3D fluorescent objects based on simulated annealing. *In* 3rd IEEE International Symposium on Biomedical Imaging: Nano to Macro, 2006. Institute of Electrical and Electronics Engineers, New York. 1020–1023.

Rea, R., J. Li, A. Dharia, E.S. Levitan, P. Sterling, and R.H. Kramer. 2004. Streamlined synaptic vesicle cycle in cone photoreceptor terminals. *Neuron.* 41:755–766. http://dx.doi.org/10.1016/S0896-6273(04)00088-1

Richards, D.A., J. Bai, and E.R. Chapman. 2005. Two modes of exocytosis at hippocampal synapses revealed by rate of FM1-43 efflux from individual vesicles. *J. Cell Biol.* 168:929–939. http://dx.doi.org/10.1083/jcb.200407148

Rizzoli, S.O., and W.J. Betz. 2004. The structural organization of the readily releasable pool of synaptic vesicles. *Science.* 303:2037–2039. http://dx.doi.org/10.1126/science.1094682

Rothman, J.S., L. Kocsis, E. Herzog, Z. Nusser, and R.A. Silver. 2016. Physical determinants of vesicle mobility and supply at a central synapse. *eLife.* 5:e15133. http://dx.doi.org/10.7554/eLife.15133

Ryan, T.A., H. Reuter, B. Wendland, F.E. Schweizer, R.W. Tsien, and S.J. Smith. 1993. The kinetics of synaptic vesicle recycling measured at single presynaptic boutons. *Neuron.* 11:713–724. http://dx.doi.org/10.1016/0896-6273(93)90081-2

Sankaranarayanan, S., and T.A. Ryan. 2000. Real-time measurements of vesicle-SNARE recycling in synapses of the central nervous system. *Nat. Cell Biol.* 2:197–204.

Shtrahman, M., C. Yeung, D.W. Nauen, G.Q. Bi, and X.L. Wu. 2005. Probing vesicle dynamics in single hippocampal synapses. *Biophys. J.* 89:3615–3627. http://dx.doi.org/10.1529/biophysj.105.059295

Südhof, T.C. 2012. The presynaptic active zone. *Neuron.* 75:11–25. http://dx.doi.org/10.1016/j.neuron.2012.06.012

Thurner, P., I. Gsandtner, O. Kudlacek, D. Choquet, C. Nanoff, M. Freissmuth, and J. Zezula. 2014. A two-state model for the diffusion of the A2A adenosine receptor in hippocampal neurons: agonist-induced switch to slow mobility is modified by synapse-associated protein 102 (SAP102). *J. Biol. Chem.* 289:9263–9274. http://dx.doi.org/10.1074/jbc.M113.505685

Tokuoka, H., and Y. Goda. 2006. Myosin light chain kinase is not a regulator of synaptic vesicle trafficking during repetitive exocytosis in cultured hippocampal neurons. *J. Neurosci.* 26:11606–11614. http://dx.doi.org/10.1523/JNEUROSCI.3400-06.2006

Wang, T., S. Martin, A. Papadopulos, C.B. Harper, T.A. Mavlyutov, D. Niranjan, N.R. Glass, J.J. Cooper-White, J.B. Sibarita, D. Choquet, et al. 2015. Control of autophagosome axonal retrograde flux by presynaptic activity unveiled using botulinum neurotoxin type a. *J. Neurosci.* 35:6179–6194. http://dx.doi.org/10.1523/JNEUROSCI.3757-14.2015

Westphal, V., S.O. Rizzoli, M.A. Lauterbach, D. Kamin, R. Jahn, and S.W. Hell. 2008. Video-rate far-field optical nanoscopy dissects synaptic vesicle movement. *Science.* 320:246–249. http://dx.doi.org/10.1126/science.1154228

Wilhelm, B.G., S. Mandad, S. Truckenbrodt, K. Kröhnert, C. Schäfer, B. Rammner, S.J. Koo, G.A. Claßen, M. Krauss, V. Haucke, et al. 2014. Composition of isolated synaptic boutons reveals the amounts of vesicle trafficking proteins. *Science.* 344:1023–1028. http://dx.doi.org/10.1126/science.1252884

Yeung, C., M. Shtrahman, and X.L. Wu. 2007. Stick-and-diffuse and caged diffusion: A comparison of two models of synaptic vesicle dynamics. *Biophys. J.* 92:2271–2280. http://dx.doi.org/10.1529/biophysj.106.081794

Zenisek, D., J.A. Steyer, M.E. Feldman, and W. Almers. 2002. A membrane marker leaves synaptic vesicles in milliseconds after exocytosis in retinal bipolar cells. *Neuron.* 35:1085–1097. http://dx.doi.org/10.1016/S0896-6273(02)00896-6